CHALMERS

# Modeling of phase transformations and cyclic plasticity in pearlitic steels

BJÖRN ANDERSSON

Department of Industrial and Materials Science
CHALMERS UNIVERSITY OF TECHNOLOGY
Göteborg, Sweden 2021

THESIS FOR THE DEGREE OF LICENTIATE OF ENGINEERING IN SOLID AND STRUCTURAL MECHANICS

# Modeling of phase transformations and cyclic plasticity in pearlitic steels

BJÖRN ANDERSSON

Department of Industrial and Materials Science
Division of Material and Computational Mechanics
CHALMERS UNIVERSITY OF TECHNOLOGY

Göteborg, Sweden 2021

Modeling of phase transformations and cyclic plasticity in pearlitic steels
BJÖRN ANDERSSON

© BJÖRN ANDERSSON, 2021

Thesis for the degree of Licentiate of Engineering
Report number: IMS-2021-24

Department of Industrial and Materials Science
Division of Material and Computational Mechanics
Chalmers University of Technology
SE-412 96 Göteborg
Sweden
Telephone: +46 (0)31-772 1000

Chalmers Reproservice
Göteborg, Sweden 2021

Modeling of phase transformations and cyclic plasticity in pearlitic steels
BJÖRN ANDERSSON
Department of Industrial and Materials Science
Division of Material and Computational Mechanics
Chalmers University of Technology

# Abstract

The low rolling resistance in railway transportation is a key factor for its high efficiency, but it comes at the price of very high contact pressure between the rail and wheel. Due to the high stresses and the large number of load cycles during railway operation, both the rail and the wheel can be susceptible to fatigue crack initiation and propagation. Furthermore, thermal loads due to frictional heating can generate high temperature in the material surface layers leading to gradual or drastic changes in material behavior. Other events that may cause such high temperatures include welding or grinding of the rail.

In this thesis, a modeling framework for phase transformations and cyclic plasticity of pearlitic steel is developed. The framework allows for modeling of the thermo-mechanical behavior of the individual phases. The implemented phase transformation kinetics in heating events include austenitization and possible tempering of martensite, and in cooling events the formation of pearlite, bainite, and martensite. Cyclic plasticity is incorporated in the model by using a Chaboche plasticity model with a von Mises yield function, non-linear isotropic and kinematic hardening. The capability of the modeling framework is demonstrated by studying the development of residual stresses during a double wheel flat scenario on the tread of a railway wheel followed by rolling contact loadings.

Further, the modeling framework is extended and improved by accounting for transformation induced plasticity (TRIP). To further improve the model, the influence of the choice of homogenization method is evaluated. Four methods are considered; iso-strain, iso-stress, self-consistent method and the linear mixture rule. These show different behavior during the multi-phase stages in simulations of a laser heated rail surface, which in turn affects the residual stress states. Although the conclusions are not entirely clear, comparison with experimental data indicates that the iso-strain and the self-consistent method are the most promising, with a slight advantage to the latter.

The thesis also presents an attempt at using the developed material model and the linear mixture rule in a simple butt-weld simulation, which can be seen as a first step towards simulation of repair welding of rails. The simulation includes a moving heat source and continuous addition of filler material. Preliminary results show that residual stress fields found for similar examples in the literature can be reproduced. Therefore, it is believed that the simulation methodologies developed in Papers A and B can be used as a basis for future developments towards simulations of repair welding of rails.

Keywords: Pearlitic steel, Phase transformations, Homogenization, Cyclic plasticity, TRIP, FEM

# Preface

The research presented in this thesis was carried out during the period of April 2019 to November 2021 at the department of Industrial and Materials Science at Chalmers University of Technology within the research project MU37 "Numerical simulations of welding and other high-temperature processes". The current study is part of the ongoing activities within CHARMEC – Chalmers Railway Mechanics (`www.chalmers.se/charmec`). Parts of the study have been funded from the European Union's Horizon 2020 research and innovation programme in the project In2Track2 and In2Track3 under grant agreement Nos 826255 and 101012456.

All numerical computations performed in the research work were enabled by resources provided by the Swedish National Infrastructure for Computing (SNIC) at Chalmers Centre for Computational Science and Engineering (C3SE) partially funded by the Swedish Research Council through grant agreement no. 2018-05973.

# Acknowledgements

First of all, I would like to thank my supervisors, Professor Magnus Ekh, Professor Johan Ahlström, and Professor Lennart Josefson. I am forever grateful that you gave me this unbelievable opportunity of this PhD-student position. Thank you for all your generous help and priceless knowledge sharing along the way to get to where we are today. I genuinely enjoy working with you and could not have done any of this without you.

I want to thank our CHARMEC research partners at Trafikverket, voestalpine, Bombardier, Lucchini and SJ for their valuable input during our interesting workshops and meetings.

I would also like to take the opportunity to thank all my friends and colleagues at the Division of Material and Computational Mechanics and the Division of Dynamics for the pleasant working environment, the interesting discussions and most of all for the daily laughter we share.

A heartfelt thanks goes out to my friends and family for their kind support. And last but not least, I want to thank my girlfriend Katarina, thank you for all the love and encouragement you surround me with.

Göteborg, November 2021
Björn Andersson

# Thesis

This thesis consists of an extended summary and the following appended papers:

**Paper A** Ali Esmaeili, Johan Ahlström, Björn Andersson, Magnus Ekh, Modelling of cyclic plasticity and phase transformations during repeated local heating events in rail and wheel steels. *International Journal of Fatigue* 151 (2021), 106361.

**Paper B** Björn Andersson, Johan Ahlström, Magnus Ekh, Lennart B Josefson, Homogenization based macroscopic model of phase transformations and cyclic plasticity in pearlitic steel. *Submitted for international publication*

The appended papers were prepared in collaboration with the co-authors. The author of this thesis contributed as follows: Paper A: took part in the implementation and simulations with the numerical models as well as in writing of the paper. Paper B: responsible for the major progress of the work, i.e., planning of the paper, developing the theory, performing numerical implementations and numerical calculations, and writing of the paper.

# Contents

# Part I
# Extended Summary

# 1 Introduction

## 1.1 Background and motivation

The historical impact that railway networks have had on shaping our modern society can hardly be understated, a simple and powerful example is the introduction of the standard time system. In regions where railways were first constructed on a large scale, Western Europe, Japan and North America, the development of track networks played a major role in economic development by considerably improving the efficiency of inland transportation. This efficiency advantage over road transportation is still its primary asset, cf. Rodrigue et. al [1].

Recent studies by Doll et al.[2] carried out on request from the European Environment Agency show that traveling by train has the lowest environmental footprint in terms of $CO_2$ emissions per kilometers traveled and per tonne transported. This is especially true for inland freight transportation, where emissions per tonne transported are about tenfold less than that of road-going heavy goods vehicles. The studies also show that during the period 2014 to 2018, railway transportation has improved its efficiency by about 13% and has increased demand, with the average European passenger train occupancy rate increasing by 12% and the load for rail freight increasing by 9%.

To limit the global climate change, the EU and the international community have agreed upon goals to reduce emissions by 80-95% below 1990 levels by 2050 (EC2011 [3]). Analysis shows that to meet this goal, the transport sector has to reduce its emissions of greenhouse gases by 60% below 1990 levels, which corresponds to cutting emissions by 70% below 2008 levels (EC2011 [4]). To this end, the reports state that a shift towards rail and waterborne transportation modes is crucial, which in turn implies the need for an efficient and reliable railway network to supply services over both short and long distances.

To continue to improve the competitiveness of train transportation, the current trends point towards traffic at higher speeds, with higher axle loads and greater traffic density. Each of these elements will increase damage and wear of the track system, which in turn increase the need and cost of maintenance. By 2012's estimate, the total annual cost for railway infrastructure maintenance and renewal in Europe was between 15 and 25 billion Euros (EECW GROUP [5]), which corresponds to about 70 000 Euros per kilometer of track, cf. Lidén and Joborn [6]. Although rail damage data from Trafikverket [7] shows that the number of rail fractures in Swedish railways have decreased from 80 to 50 fractures per year during the period from 2014 to 2020, it also shows that more than 33% of the fractures occur in welds. Hence there are strong economic and environmental incentives for improving maintenance actions and their planning.

The low rolling resistance in the wheel-rail contact is a key factor for the high efficiency of railway transportation, but it comes at the price of very high contact pressure between

the rail and wheel. The rolling contact loading results in a multiaxial stress state in terms of a combination of compression and shear, and gives rise to both cyclic plasticity and fatigue damage. Due to the high load magnitude and the large number of load cycles during railway operation, the wheel and rail can be susceptible to high cycle fatigue, whereby fatigue damage can have devastating consequences. A critical case is the formation of brittle martensite, which can occur if the temperature in the rail or wheel steel is increased to austenitization temperature levels and followed by rapid cooling. Examples of events that may cause such temperatures include severe braking inducing wheel slip or improperly performed maintenance actions (such as rail grinding and rail repair welding).

In the centre of excellence in railway mechanics at Chalmers (CHARMEC), local temperature driven phase transformations of pearlitic railway steel and the resulting residual stress-strain state have been studied both experimentally, cf. Jessop [8], Niederhauser et al. [9], Ahlström and Karlsson [10], and using numerical simulation tools, cf. Esmaeli et al. [11], Jergeus [12], Ahlström and Karlsson [13]. The studies confirm that these local high temperature events can have detrimental effects on the structural integrity of railway components. The studies also recognize the importance of accurate simulation models to assess the consequences during railway operation conditions. Therefore, to improve the fidelity of the simulation results there is a need to further develop the modeling, e.g. regarding the coupling between the phase transformations and the temperature-dependent cyclic mechanical behavior. There is also a need enable large-scale simulations to study how the residual state from thermal processes is affect by repeated mechanical contact loading.

## 1.2 Research objectives

The work presented in this thesis has been performed in the CHARMEC project MU37- "Welding and other high temperature operations in steel". It is an effort towards improving the simulation tools used for simulating high temperature operations in railway steel. The research objectives of this licentiate thesis and the research project financing this work are:

- Develop thermo-mechanical material models of phase transformations and cyclic plasticity in pearlitic railway rail and wheel steels. The goal is to use the models to predict residual stress evolution and fatigue crack initiation in railway applications. The models should be based on, and validated against, experimental data.
- Investigate and analyze basic assumptions in the formulation of the thermo-mechanical material models and, if needed, improve upon these by extending available models found in the literature to account for phenomena observed in experiments. Examples that have been explored in this thesis are the assumption of the homogenization method, the phenomenon of transformation induced plasticity, and the importance of accounting for cyclic plasticity.
- Implement models in a finite element framework that can be used to simulate processes in railway applications such as thermal heating events (e.g. braking of

railway wheels) and maintenance operations of rails such as grinding and welding. In particular, the implementations should be used to study how the material state resulting from such heating events is changed during operational conditions.

- Study the process of rail repair welding. This process is fundamentally different from the flash butt welding or alumino-thermic (thermite) welding used when laying the track, as it involves cyclic and more local thermal loads with less heat input. Besides, it has not been studied to the same extent.

- The overall goal is that the research will lead to accurate and predictive methods to support and improve technology development and reduce life cycle cost (LCC) in the railway industry. The outcome, i.e. the simulations tools, should also aid in designing maintenance procedures to reduce the risk for fatigue failure and excessive wear.

## 1.3 Pearlitic railway steel

The production of everything metal involves heating and cooling during one or multiple stages of the manufacturing process. For steel alloys, this entails not only liquid to solid phase transformations but also solid to solid phase transformations. For the latter, the base metal of steel, iron, takes on different crystalline structures depending on the temperature and its rate of change. In interaction with alloying elements, this gives different steel grades a wide range of properties, as shown in the strength and ductility illustration in Figure 1.1. The interstitial carbon solutes in the iron lattice as well as carbides forming play a key role during deformation as they impede dislocation movement, thus hardening the material. Carbon is also a crucial element during phase transformations as the respective crystalline structures have different solubility of carbon. For example, the face-center cubic (FCC) structure of the austenite phase, stable at high temperatures, holds more interstitial carbon than the body-center cubic (BCC) structure of the ferrite phase, stable at low temperatures. Therefore, during the cooling of austenite with a eutectoid chemical composition (ca 0.7 weight-percent carbon) under rather slow cooling rates, it transforms into the two-phase microstructure of pearlite which is a lamellar microstructure consisting of ferrite and cementite, where the carbon is bound in the cementite phase which has the atomic composition $Fe_3C$, see e.g. Bhadeshia [14] and Pereloma and Edmonds [15].

The strong laminar network of ferrite and cementite makes pearlite ductile and relatively wear resistant, making it suitable for railway applications. However, to form pearlitic microstructure from austenite slow cooling rates are required. If the austenite is subjected to moderate cooling rates or quenching, there is not enough time for the interstitial carbon solutes to diffuse out of the austenite FCC crystal structure in large enough quantities to form cementite, whereby the metastable microstructures of bainite or martensite are formed, cf. Raabe [17] and Lin et al. [18].

During rail manufacturing, the applied heat is controlled and regulated such that a macroscopically homogeneous microstructure is generated without introducing significant residual stresses. However, if the heating is not applied to the entire rail but focused on a

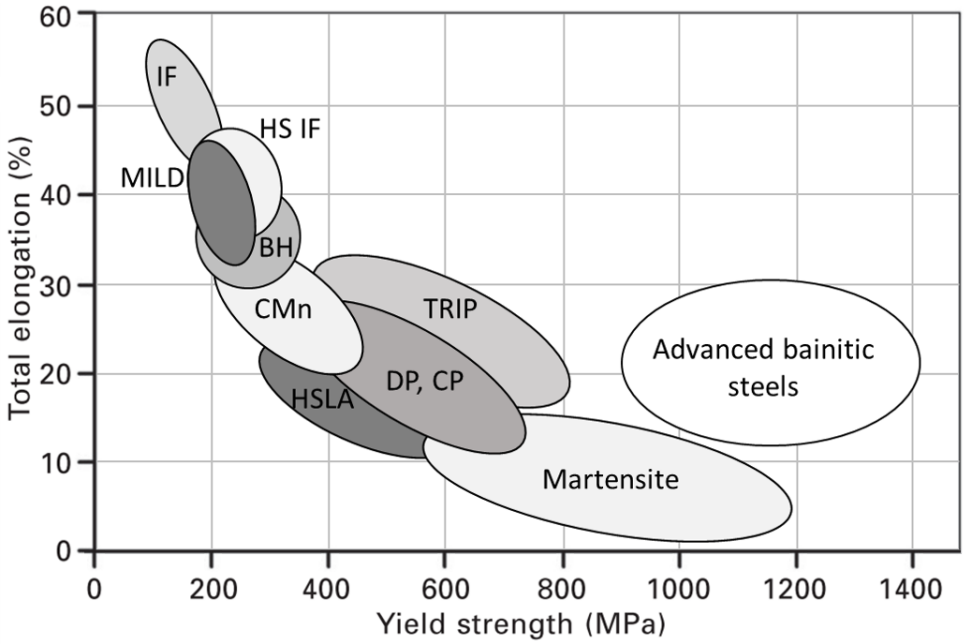


Figure 1.1: *Total elongation and Yield strength, illustrating strength and ductility of different commercial steels; IF - interstitial free, HS IF - High strength interstitial free, MILD - Mild steel (low carbon steel), BH - bake hardening, CMn - Structural steel, HSLA - High strength low alloy, DP - Dual phase, CP - Complex phase, TRIP - Transformation induced plasticity. Image from Pereloma and Edmonds [16].*

small spot, phase transformations may occur if the cooling is not regulated. For rapid cooling of the heated spot, the resulting material state might no longer be homogeneous pearlite, but a region of bainite or martensite. This local region will then be subjected to significant residual straining and does not have the ductile material properties of the surrounding unaffected pearlite. Examples of operations that may cause local heating events of sufficiently high temperatures (above austenitization temperature) and rapid cooling are welding, grinding, thermal cutting and severe train wheel braking.

In order to accurately analyze the mechanical residual state following these events by numerical simulation, both the inhomogeneous material properties and residual stress state must be accounted for. Papers A and B present material models and a simulation methodology accounting for the thermal load history, i.e. the cyclic thermal straining, phase transformations and corresponding change of material characteristics caused by local heating events of pearlitic railway steel. The adopted phase transformation kinetics, cyclic plasticity modeling of each phase and homogenization of the individual phase behavior are summarized in the following sections.

## 1.4 Phase transformation kinetics

The main phases of a low alloy carbon steel considered in this study are ferrite, pearlite, austenite, cementite, bainite and martensite. Note that this work makes no strict distinction between phase or microstructure, all different fundamental forms of steel are referred to as phases, even though e.g. pearlite is in fact a microstructure which is a combination of the two phases ferrite and cementite. At a given constant temperature and a known carbon content, the iron-carbon phase diagram gives the stable equilibrium phase, e.g. austenite or ferrite. Metastable phases, such as martensite and bainite, nucleate as the steel is subjected to high rates of temperature change. Paper A presents a detailed phase transformation kinetic framework where the following phase transformations are considered during heating and cooling:

- *Heating:* Austenitization of ferrite, pearlite, cementite and bainite
- *Cooling:* Austenite to ferrite, pearlite, cementite, bainite or martensite
- *Re-heating of martensite:* Martensite tempering and decomposition to ferrite and cementite

The nucleation of austenite, i.e. austenitization, is a diffusive transformation that occurs upon heating above the austenite transformation temperature. Higher heating rates result in higher austenitization temperature, cf. Archard et al. [19]. The kinetics of the transformation is presented in IT-diagrams and is, for a constant temperature, described by the Avrami (JMAK) equation, cf. Denis et al. [20] and Fernandes et al. [21]. However, to account for variations in temperature during the transformation, Scheil's [22] additive rule can be adopted, cf. Verdi and Visintin [23].

Generally, slow cooling of hypoeutectoid steel in austenitic form produces a ferritic-pearlitic microstructure. Whereas slow cooling of austenite in eutectoid steel yields fully pearlitic microstructures and in the case of hypereutectoid steel, cementite nucleate in the austenite grain boundaries, and the interior of the grains becomes pearlitic. At moderate cooling rates there is less time for diffusion to occur and carbon will be finer dispersed, forming a partly bainitic microstructure. As these transformations can be considered diffusive, the JMAK equation and Scheil's additive rule can be used to quantify the phase fraction evolution.

At high cooling rates, i.e. quenching, there is insufficient time for diffusive phase transformations to occur, generating unstable austenite at lower temperatures followed by a diffusionless martensitic transformation. This transformation is modeled as purely temperature dependent following Koistinen-Marburger [24] equation.

The constitutive phase transformation framework presented in Paper A also considers tempering of martensite. Tempered martensite is modeled as an individual phase and its transformation is modeled as only dependent on temperature, based on the dilatometry experiment by Cvetkovski et al. [25].

## 1.5 Cyclic plasticity material model

A Chaboche plasticity model, cf. Chaboche [26], has been adopted and calibrated by Esmaeili et al. [11] to fit cyclic experimental data at different temperatures for the pearlitic ER7 steel (EN13262 [27]). The experiments are isothermal low-cycle fatigue tests for temperatures ranging from room temperature to 625°C. This model and its material parameters were used as starting point for the material modeling of the different phases in Paper A. For the model to account for multi-phase stages, i.e. stages when more than one phase exists, each phase is modeled by its individual constitutive model, and homogenization is used to compute the total response (as will be discussed in Subsection 1.6). This section presents a brief summary of the Chaboche plasticity model extended with transformation induced strain adopted for all the individual phases.

For the small strain setting, the total strain $\boldsymbol{\epsilon}$ for each individual phase is assumed to be additively decomposed into the following parts (see e.g. Mahnken et al. [28]):

$$\boldsymbol{\epsilon} = \boldsymbol{\epsilon}^{\mathrm{e}} + \boldsymbol{\epsilon}^{\mathrm{th}} + \boldsymbol{\epsilon}^{\mathrm{tv}} + \boldsymbol{\epsilon}^{\mathrm{p}} + \boldsymbol{\epsilon}^{\mathrm{tp}} \tag{1.1}$$

where $\boldsymbol{\epsilon}^{\mathrm{e}}$ is the elastic strain, $\boldsymbol{\epsilon}^{\mathrm{th}}$ the thermal expansion strain, $\boldsymbol{\epsilon}^{\mathrm{tv}}$ the transformation strain, $\boldsymbol{\epsilon}^{\mathrm{p}}$ the plastic strain, and $\boldsymbol{\epsilon}^{\mathrm{tp}}$ the strain due to transformation induced plasticity (TRIP). The model was extended from Paper A to Paper B by including the TRIP strain. The elastic strain $\boldsymbol{\epsilon}^{\mathrm{e}}$ governs the stress $\boldsymbol{\sigma}$ the phase is subjected to, whereby the stress $\boldsymbol{\sigma}$ can be computed using linear isotropic elasticity by adopting Hooke's law. The stress is assumed to be decomposed into a deviatoric and a volumetric part:

$$\begin{aligned} \boldsymbol{\sigma} &= \boldsymbol{\sigma}_{\mathrm{dev}} + 1/3\,\sigma_{\mathrm{vol}}\,\boldsymbol{I} \\ \boldsymbol{\sigma}_{\mathrm{dev}} &= \mathbf{I}_{\mathrm{dev}} : \boldsymbol{\sigma} = 2\,G\,\boldsymbol{\epsilon}^{e}_{\mathrm{dev}} \\ \sigma_{\mathrm{vol}} &= \boldsymbol{I} : \boldsymbol{\sigma} = 3\,K_{\mathrm{b}}\,\epsilon^{e}_{\mathrm{vol}} \end{aligned} \tag{1.2}$$

where $G$ is the shear modulus and $K_{\mathrm{b}}$ the bulk modulus, both phase specific, temperature dependent material parameters.

The von Mises yield function is used to distinguish elastic and plastic response:

$$\Phi = \sqrt{\frac{3}{2}}|\boldsymbol{\sigma}_{\mathrm{dev}} - \boldsymbol{X}| - (R + \sigma_Y) \tag{1.3}$$

where $R$ is the isotropic hardening stress, $\boldsymbol{X}$ is the total kinematic hardening stress (back-stress), and $\sigma_Y$ is the initial yield stress. The total kinematic hardening stress is obtained from adding multiple back-stresses, each following the Armstrong Frederick [29] evolution law for kinematic hardening. The chosen number of back-stresses depends on how many are needed to predict the experimental data, e.g. Nikas et al. [30] and Cvetkovski et al. [25], with sufficient accuracy. In the model for pearlite presented by Esmaeili at al. [11], three back-stresses were used. As a complement to experimental data for pearlite the software JMatPro [31] was used to identify parameter values.

## 1.6 Homogenization

For a multi-phase material, the overall constitutive behavior can be obtained from homogenization of the behavior of the individual phases, see e.g. Simsir et al. [32] and Mahnken et al. [28]. The most common homogenization method for phase transformation simulations found in the literature is the linear mixture rule, see e.g. Denis et al. [33] and Fisher et al. [34]. But there are also non-linear mixture rules presented in the literature, see e.g. Stringfellow et al. [35] and Bouaziz and Buessler [36], where it is shown that linear mixture rules may not be sufficiently capable of replicating experimental material behavior.

In Paper B we adopt and compare results for four homogenization methods: isostrain, isostress, a self-consistent model and the linear mixture rule. The linear mixture rule is the most straightforward way of handling multi-phase states in steel, see e.g. Ahlström and Karlsson [13] and Fischet et al. [34], since it does not require individual material models for the phases. By this method, the material model parameter values are taken as the phase fraction scaled average. For example, the fourth-order stiffness tensor $\mathbf{E}^e$ is computed as follows:

$$\mathbf{E}^e = \sum_{x=1}^{n_x} p_x \mathbf{E}_x^e \tag{1.4}$$

Note that the sum of phase volume fractions, $p_x$, equals 1 and that the temperature and phase fractions are assumed to remain constant during each time increment of the mechanical problem.

In the other homogenization methods used in Paper B, this assumption allows for homogenized strain and stress to be computed from phase fraction scaled averages of the individual strains and stresses as follows:

$$\mathrm{d}\bar{\boldsymbol{\epsilon}} = \sum_{x=1}^{n_x} p_x \, \mathrm{d}\boldsymbol{\epsilon}_x \qquad \mathrm{d}\bar{\boldsymbol{\sigma}} = \sum_{x=1}^{n_x} p_x \, \mathrm{d}\boldsymbol{\sigma}_x \tag{1.5}$$

For the isotrain (Voigt) homogenization method all phases are assumed to have the same strain increment, i.e. $\mathrm{d}\boldsymbol{\epsilon}_x = \mathrm{d}\bar{\boldsymbol{\epsilon}}$. Therefore, the homogenized stress increment can be obtained as follows:

$$\mathrm{d}\bar{\boldsymbol{\sigma}} = \sum_{x=1}^{n_x} p_x \, \mathbf{E}_x : \left(\mathrm{d}\boldsymbol{\epsilon}_x - \mathrm{d}\boldsymbol{\epsilon}_x^{\mathsf{th}} - \mathrm{d}\boldsymbol{\epsilon}_x^{\mathsf{tv}}\right) = \sum_{x=1}^{n_x} p_x \, \mathbf{E}_x : \left(\mathrm{d}\bar{\boldsymbol{\epsilon}} - \mathrm{d}\boldsymbol{\epsilon}_x^{\mathsf{th}} - \mathrm{d}\boldsymbol{\epsilon}_x^{\mathsf{tv}}\right) \tag{1.6}$$

where $\mathbf{E}_x$ is the tangent stiffness. Similarly for the isostress (Reuss) homogenization method, all phases are assumed to have the same the stress increment, i.e. $\mathrm{d}\boldsymbol{\sigma}_x = \mathrm{d}\bar{\boldsymbol{\sigma}}$. Hence, the homogenized strain increment can be obtained as:

$$\mathrm{d}\bar{\boldsymbol{\epsilon}} = \sum_{x=1}^{n_x} p_x \, \left(\mathbf{E}_x^{-1} : \mathrm{d}\bar{\boldsymbol{\sigma}} + \mathrm{d}\boldsymbol{\epsilon}_x^{\mathsf{th}} + \mathrm{d}\boldsymbol{\epsilon}_x^{\mathsf{tv}}\right) \tag{1.7}$$

However, since the model is used in a strain increment driven FEM algorithm the homogenized stress increment $\mathrm{d}\bar{\boldsymbol{\sigma}}$ is unknown. Therefore, an additional Newton iteration

scheme is needed to satisfy the isostress assumption, $\mathrm{d}\boldsymbol{\sigma}_x = \mathrm{d}\overline{\boldsymbol{\sigma}}$, while fulfilling the homogenized strain increment (Equation 1.5), see Paper B.

In the self-consistent homogenization method, neither the strain nor stress increment is prescribed. The method builds on Eshelby's [37] solution of an elastic ellipsoidal inclusion in an infinite elastic body. Each phase is assumed to be the inclusion and the surrounding body is assumed to be the homogenized state. The stress, strain, and displacement fields of each phase are thereby affected by the homogenized state. Originally formulated for elasticity, the method is extended to plasticity by Hutchinson [38]. In this method, the strain increment in each phase $\mathrm{d}\boldsymbol{\epsilon}_x$ can be expressed as:

$$\mathrm{d}\boldsymbol{\epsilon}_x = \mathbf{A}_x : \mathrm{d}\bar{\boldsymbol{\epsilon}} \tag{1.8}$$

with the fourth order concentration tensor $\mathbf{A}_x$ iteratively computed based on the Eshelby tensor, see e.g. Lebensohn et al. [39]. The homogenized stress increment can then be computed similarly to that of the isostrain method (see Equation 1.6):

$$\mathrm{d}\overline{\boldsymbol{\sigma}} = \sum_{x=1}^{n_x} p_x \, \mathbf{E}_x : \left(\mathrm{d}\boldsymbol{\epsilon}_x - \mathrm{d}\boldsymbol{\epsilon}_x^{\mathsf{th}} - \mathrm{d}\boldsymbol{\epsilon}_x^{\mathsf{tv}}\right) = \sum_{x=1}^{n_x} p_x \, \mathbf{E}_x : \left(\mathbf{A}_x : \mathrm{d}\bar{\boldsymbol{\epsilon}} - \mathrm{d}\boldsymbol{\epsilon}_x^{\mathsf{th}} - \mathrm{d}\boldsymbol{\epsilon}_x^{\mathsf{tv}}\right) \tag{1.9}$$

## 1.7 Thermo-mechanical finite element framework

High temperature operations in pearlitic steels involve simultaneous mechanical and metallurgical processes occurring at different time and length scales, as discussed in Section 1.3. Most of the different aspects and phenomena of the couplings between these processes can be accounted for by using the finite element method (FEM). Figure 1.2 presents a schematic view of the couplings between the processes, described in greater detail by e.g. Coret and Combescure [40] and Börjeson and Lindgren [41]. Several works, e.g. Lindgren [42] and Dong [43], have shown that several simplifications of these interacting couplings can be made without significant loss of accuracy in the simulation results.

In Papers A and B we have adopted a decoupling of the thermo-mechanical analysis into a transient thermal analysis and a quasi-static structural analysis. The temperature field from the thermal analysis drives the metallurgical processes, i.e. the phase transformation kinetics described in Section 1.4. Transformation strain $\boldsymbol{\epsilon}^{\mathrm{tv}}$, TRIP strain $\boldsymbol{\epsilon}^{\mathrm{tp}}$ (in Paper B) and thermal strain $\boldsymbol{\epsilon}^{\mathrm{th}}$, marked by green arrows in Figure 1.2, together with mechanical loading drive the response in the mechanical finite element analysis. Figure 1.2 also shows grey arrows recognizing couplings not accounted for the model implemented in Papers A and B. Out of these simplifications it is, based on literature see eg. Edalatpour et.al [44], believed that omitting the latent heat has the largest impact on the accuracy of the simulations. However, this should be more carefully investigated in future work.

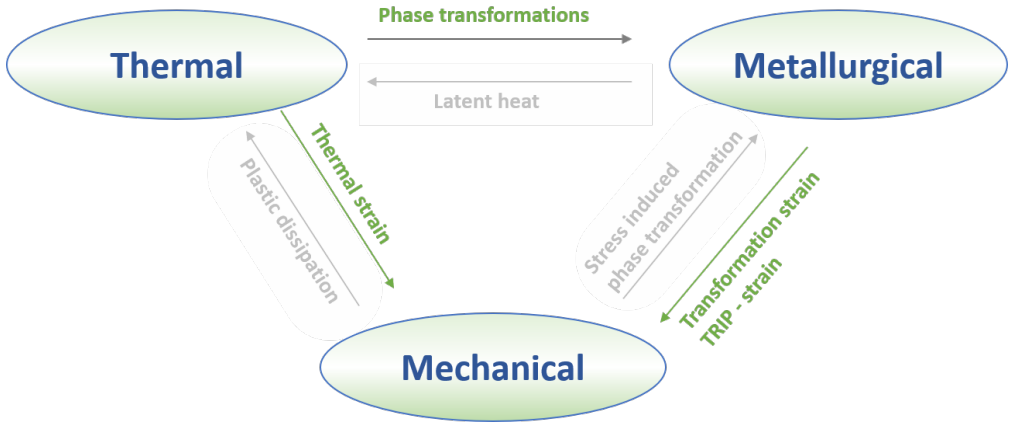


Figure 1.2: *Coupling mechanisms between thermal field, microstructure evolution and mechanical field in the adopted thermo-mechanical simulation methodology. Mechanisms written with green text is accounted for while mechanisms written with grey text are not accounted for in this work.*

## 1.8 Summary and selected results from appended papers

### 1.8.1 Paper A

In Paper A, the FE-implementation of the phase transformation kinetics and cyclic plasticity material model (briefly presented in Sections 1.4 and 1.5) is demonstrated in a simulation of a scenario of a double wheel flat in a railway wheel. In this paper, the isostrain homogenization method is adopted but no TRIP effect is accounted for.

In a single wheel flat scenario, the brake locks and the wheel skids along the rail causing intense frictional heat input on a small contact patch. As the wheel starts rolling again, the wheel tread is subjected to traversing rolling contact loading and the rapid heat conduction can cause martensitic phase transformation. In the event of a double wheel flat the loading scenario is repeated. This example demonstrates the capability of the model to simulate both cyclic phase transformations and to predict how the resulting residual stresses are affected by the subsequent cyclic mechanical load. These are key aspects when evaluating the risk of crack formation in the brittle martensite. This section presents some of the major findings of the study performed in Paper A and a brief description of assumptions in the simulations. This is also presented in Figure 1.3.

The 3D FE model of the wheel is shown in Figure 1.3a. The loading consists of one longer heat pulse, followed by three over-rollings, followed by a second shorter heat pulse, and finally ten over rollings. The prescribed heat flux has a cut-off temperature of 1000°C and the mechanical load corresponds to 20 tonnes axle load.

The resulting temperature field from the first of the two heat pulses is presented in Figure 1.3b. Highlighted in this figure is the region shown Figure 1.3c, which presents the

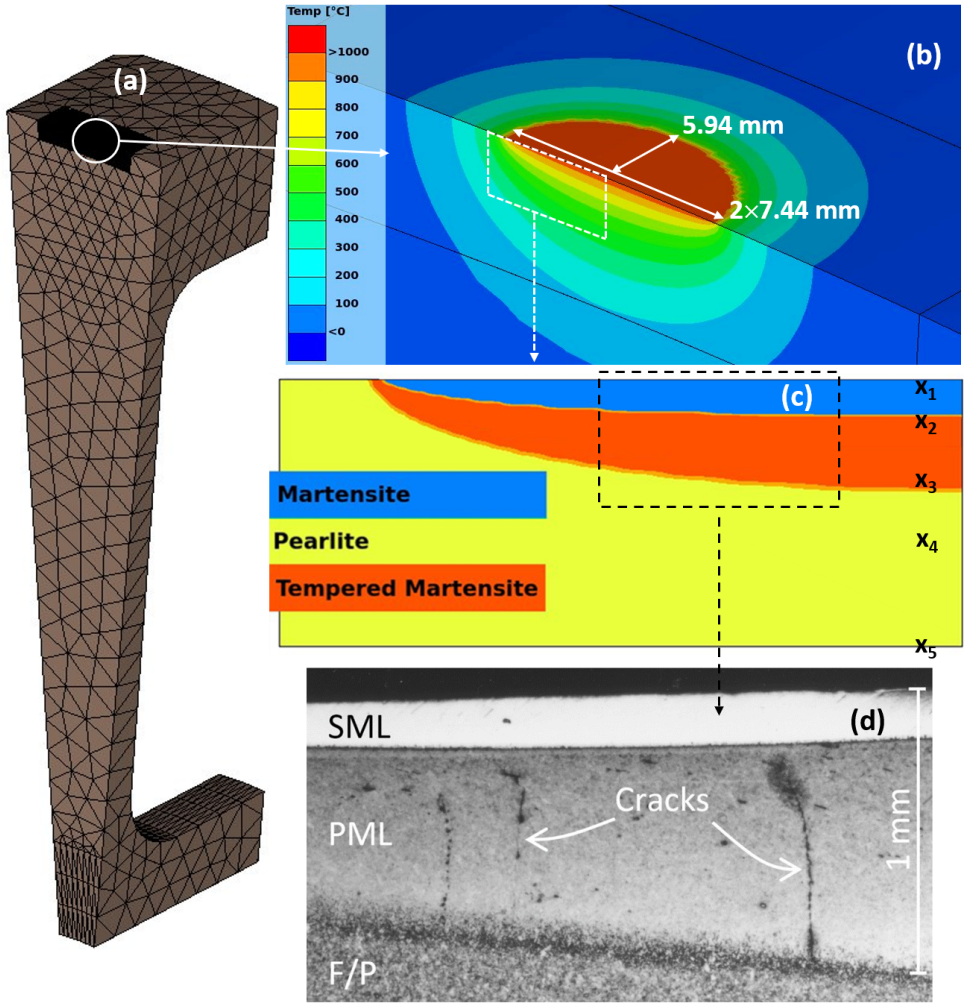


Figure 1.3: *(a) FE-model of a railway wheel, (b) one of two applied heat pulses, (c) the resulting phase transformations and four data measuring points $x_i$, and (d) comparison with experimental results from Ahlström and Karlsson [45], F/P represents the un-affected ferritic–pearlitic base material, PML the primary martensite layer and SML the secondary, tempered, martensite.*

resulting phases after two heat pulses. A larger region of tempered martensite can be observed, as well as a thinner disk of untempered martensite. As the second heat pulse is shorter than the first, the material volume that reaches austenitization temperature during this heat pulse is smaller. This results in a thinner secondary martensitic volume.

This can be compared to the experimental results from Ahlström and Karlsson [45] shown in Figure 1.3d. This cross section view through a double wheel flat shows the primary martensite layer (PML) formed by the first skidding event and the thinner, secondary martensite layer (SML) formed during a second, less intense heating event. The grey area at the bottom of the picture shows the ferritic–pearlitic (F/P) base material which is unaffected by the heating events. The similarities between experimental results and simulations show the potential for the adopted modeling framework.

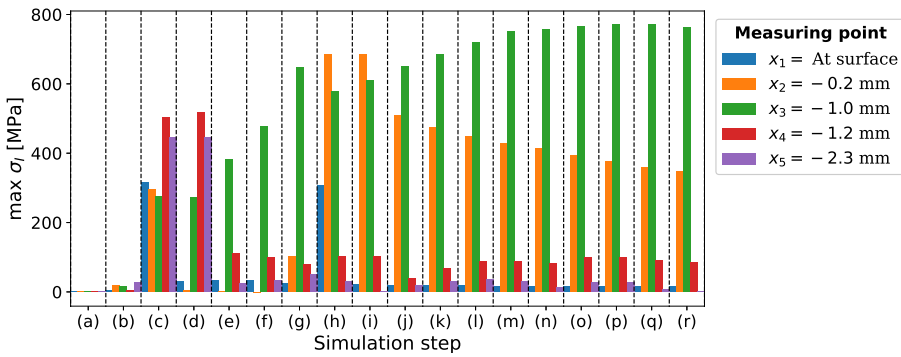


Figure 1.4: *Maximum principal stress $\sigma_I$ for each simulation step: (a) denotes the time of temperature increase to the operational temperature, (b) the first thermal heating event (c) cooling to operational temperature (d) to (f) three mechanical over-rollings (g) the second heating event (h) cooling to operational temperature (i) to (r) ten mechanical over-rollings*

Figure 1.3c also shows five points, $x_1$ to $x_5$, that are used when evaluating the stress condition in the heat affected zone during the whole process. The histogram in Figure 1.4 shows the maximum (first) principal stress, $\sigma_I$, at each point for each simulation step. The steps are the following; (a) temperature increase to the 100°C operational temperature, (b) the first heat pulse, (c) cooling to operational temperature, (d) to (f) three mechanical over-rollings, (g) the second, shorter heat pulse, (h) cooling back to operational temperature and (i) to (r) ten mechanical over-rollings. The result indicates compressive, or low tensile stresses in the secondary martensitic layer (see point $x_1$) and higher tensile stresses in the tempered, primary martensitic layer (see points $x_2$ and $x_3$). Tensile principal stresses can cause failure in the brittle tempered martensite. This can explain the small cracks that are visible in the primary martensitic layer in Figure 1.3d. The histogram also shows the stress evolution during the ten over-rollings following the second heat pulse. The trend of decreasing peak principal stress magnitude close to the surface (see measuring point $x_2$) suggests that the over-rollings are beneficial in terms of mitigating the risk of crack related failure.

### 1.8.2 Paper B

In Paper B, the modeling framework of Paper A is extended to include three additional homogenization methods; the isostress method, the self-consistent method and the linear mixture rule. In addition, the TRIP effect is accounted for. Comparison with experimental data from Mahnken et al. [28] shows that for the homogenized material behavior to generate the correct strain output, the TRIP strain $\boldsymbol{\epsilon}^{\mathrm{tp}}$, see Equation 1.1, must be included in the individual constitutive models both the austenite and martensite. Figure 1.5 presents the experiment set-up and the corresponding FE-model used to evaluate the homogenization methods. The surface of the railhead, shown in Figure 1.5a, is subjected to focused laser heating producing a small martensitic disk, as shown in Figure 1.5b. By using the 2D axisymmetric FE-model illustrated in Figure 1.5c, the laser heating procedure is simulated in uncoupled heat transfer and mechanical simulation. Figure 1.5d shows the predicted martensitic disc from the FE simulation.

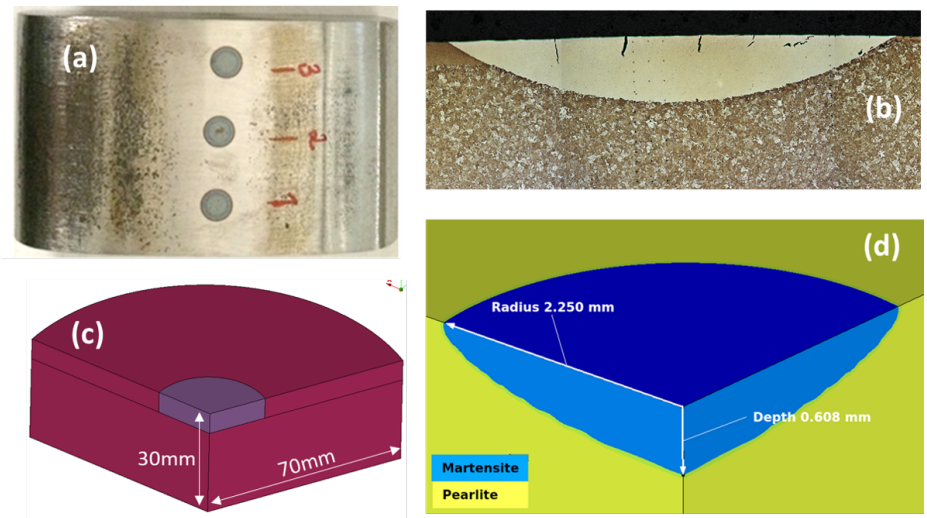


Figure 1.5: *(a) laser heated spots on the surface of a railway rail, (b) experimental results showing cross section view of laser heated spot, (c) axisymmetric FE-model, (d) simulation results showing a martensitic disc. Photographs in (a) and (b) are from Jessop [46].*

Due to the multi-phase stages of the process, the end results from the four homogenization methods differ. Figure 1.6 presents the residual stress and phase fractions after the heat has been applied and the temperature has cooled back to 20°C. The top graph presents the radial stress along the surface of the FE-model presented in Figure 1.5c, and experimental stress measurements obtained from the rail experiment by Jessop [46] presented in Figure 1.5a. The vertical lines at the experimental measurement points indicate the spread in measured data and the horizontal lines indicate the spread in where the experimental measuring point is located.

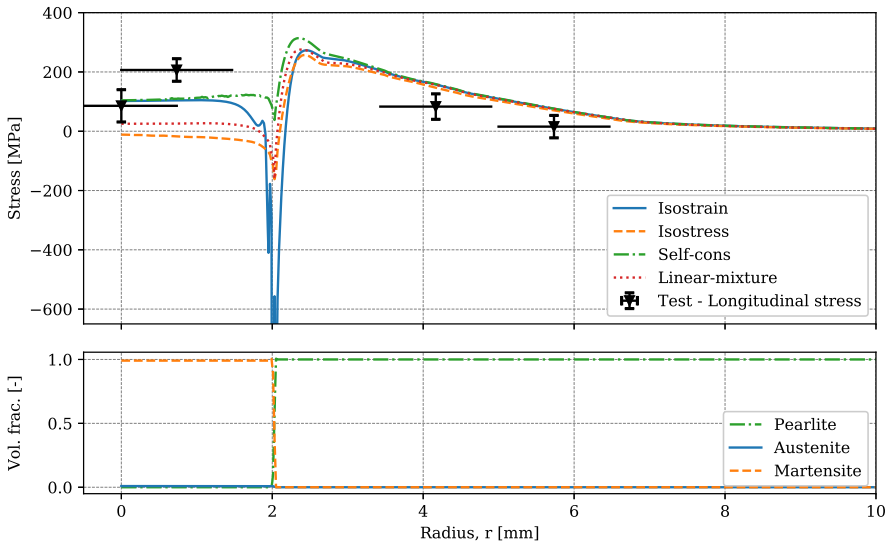


Figure 1.6: *Top graph: Residual stress obtained using different homogenization methods and experimental measurements. Bottom graph: Volume fraction and temperature at the surface of the FE-model after cooling. Experimental results are obtained from Jessop [46]*

Comparing the simulation and experimental presented in Figure 1.6 shows that none of the models is a perfect match. However, as described in Paper B, the simulation uses wheel material properties, whereas the experimental measurements are from rail steel. The cyclic plasticity properties of the steel grades are similar; the finer pearlite lamellar spacing in the wheel surface compensates for the non fully pearlitic microstructure. The phase transformation temperatures are slightly different, but there are no principal difference. Thus, it is believed that despite the different steel grades, the results are of the same order of magnitude and the overall trend is valid.

# 2 Introduction to FE welding simulations

This chapter presents an early attempt to use the material models and simulation methodology presented in Papers A and B in fusion welding simulations. The chapter starts with a general presentation of the mechanical aspects of welding in railways and a brief introduction to computational welding mechanics. Next, the constitutive model's capability for modeling basic welding principles is discussed using free dilatation and three bar experiment simulations. Finally, FEM techniques for modeling fusion welding with a moving heat source and addition of filler material are described and demonstrated for a case of single-pass butt welding of a plate.

## 2.1 Welding in railway mechanics

Welding in railway rails is typically performed for two reasons, joining the rails when laying the track and repairing damaged parts of the railhead. In Sweden, rail sections are normally first constructed by joining several rails in a stationary plant by flash butt welding. These sections are then transported to the field and joined by alumino-thermic (thermite) welding. Repair welding is generally performed using fusion welding to, layer-by-layer, fill the gap after the damaged section has been cut away. For both welding procedures, the localized heating generates rapid cooling rates in the weld and surrounding material which may cause phase transformations and result in varying hardness of the rail surface. In addition, studies of microstructural changes during flash butt welding by Porcaro et al. [47] show how grain growth and partial pearlite spheroidization decrease hardness, yield strength and tensile strength. Due to these irregularities, the welded region acts as a weak point in the track system, which can cause uneven wear and increased contact forces between the railway wheel and the track.

Studies of the residual stress field from flash butt welding, cf. Skyttebol and Josefson [48] and Tawfik et al. [49], and thermite welding, cf. Josefson et al. [50] and Salehi et al. [51], indicate high tensile residual stresses in the web of the welded rail at the weld and the interface to the rail. Moreover, the studies show that these stresses are not redistributed during typical operational loads. Hence, the residual stress state may have a detrimental effect by contributing to the growth of horizontal fatigue cracks from defects below the railhead surface, cf. Skyttebol et al. [52] and Josefson [53].

For repair welding, the multiple layers of deposited weld beads cause a more complex evolution of the stress field, compared to e.g. the intense heat input of thermite welding. As the heat input per weld pass during repair welding is lower and affects a smaller region, the cooling rates will be higher. Also, by each additional weld pass, the previous layers and surrounding region are reheated causing more pronounced cyclic straining. Therefore, there is a greater risk of both martensite formation and varying surface hardness. Efforts to study rail repair welding mechanically were made by Kabo et al. [54] and by Lee et al. [55]. Results in both these references indicate that operational rolling contact loads redistribute the residual stresses at the surface of the repaired rail, while the stress magnitudes are increased beneath the rail surface. Thus reducing the risk of crack initiation on the repaired surface, but increasing the risk for subsurface crack initiation.

## 2.2 Computational welding mechanics

The welding process is an inherent multi-physics and multi-scale transient problem, and simulations therefore require modeling of multiple overlapping physical phenomena. The many interacting phenomena of wire arc muilt-pass fusion welding are described by e.g. Runesson et al. [56]. Fortunately, when simulating welding many of these interactions are negligible compared to the interactions in what Lindgren [57] refers to as classical computational welding mechanics, i.e. only the interacting mechanisms presented in Figure 1.2. However, depending on the scope of the analysis, other interactions may need to be included, e.g. the heat source model might need to include electrical arc weld physics. The scope often involves studying the residual stress field and the resulting distortions. With this purpose, the common practice is to use analytical or numerical heat input models and not to include fluid flow together with thermo-mechanics, thereby isolating the thermal, mechanical and metallurgical phenomena and interactions, cf. Goldak and Akhlaghi [58].

By assuming that plastic dissipated energy is negligible compared to the weld arc heat input and that deformation is small enough not to affect the heat transfer at the thermal boundary conditions, the system can be considered as a one-way coupled thermo-mechanical system. Together with the assumption that the stress field does not affect the microstructure evolution (e.g. the Magee TRIP effect [59]), this allows for the heat transfer problem to be solved prior to solving the mechanical problem.

Regarding the multi-scale aspects of welding, processes on the microscopic level for the thermal, mechanical and metallurgical interactions include grain growth, dissolution and precipitation of alloying elements, changes in dislocation density and phase transformations. All these processes affect the residual state of the material in terms of e.g. hardness, strength and toughness, and depending on the scope of the analysis these can be accounted for in simulations, see e.g. Oddy et al. [60]. However, on the macroscopic level its generally only the phase transformation aspect that has to be accounted for.

Although this presentation of computational welding mechanics is brief, the work presented in Papers A and B shows several similarities to macroscopic welding simulations in terms of thermo-mechanical material modeling. However, in terms of the necessary FEM framework, welding simulations are more complex than the simulations presented in Papers A and B. Requiring intricate modeling techniques for the heat input from the moving heat source, the filler material and component geometry, which will be presented in the sections that follow.

## 2.3 Dilatation simulation

This section presents dilatation simulations and simulations of thermal expansion under uniaxial stress conditions with the purpose of examining whether the material models presented in Papers A and B possesses the basic characteristics needed for simulating welding of pearlitic steel.

Material modeling in welding simulations must be able to account for processes during both heating and cooling. The material model presented in Papers A and B includes (as discussed in Sections 1.4 to 1.8) thermal expansion, phase transformation kinetics, temperature dependent mechanical behavior and the TRIP effect (in Paper B). As an example (from Paper A), simulation and experimental result of free dilatation is shown in Figure 2.1. The simulation uses the isostrain homogenization method and the results demonstrate the capability to account for phase transformations during both heating and cooling, also the ability simulate tempering which may occur from the reheating of multiple weld passes.

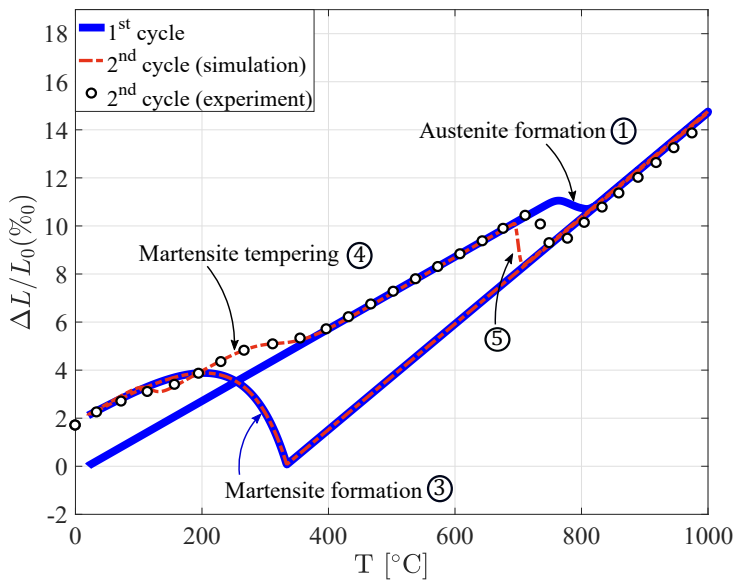


Figure 2.1: *Strain evolution when heating and cooling causes phase transformation of martensite, pearlite and austenite. Experimental data from Cvetkovski et al. [25] are shown only for the* $2^{nd}$ *heat cycle.*

In welding simulations it is important to include the TRIP effect. The thermal expansion and subsequent contraction of the weld and the heat affected zone are constrained by the surrounding non-heated material causing stresses in the heat affected material. Hence, phase transformations do not occur in a stress-free state, in contrast to the transformations shown in 2.1. Phase transformation occurring in a stressed state produces additional

strain due to the TRIP effect, see e.g Wolff et al. [61] and Fischer et al. [62], which in turn impacts the residual stress state. Including this effect in weld simulations is therefore required to obtain accurate predictions, see eg. Oddy et al. [63] and Mahnken [28]. This also seen in the simulations of thermal expansion under uniaxial stress conditions presented in Paper B.

## 2.4 Three bar experiment

Important understanding of the stress and strain development during fusion welding can be gained by studying a simple *three bar model*. This is a classic example to conceptually model the residual longitudinal stresses in a welded plate, see e.g Masubuchi [64] and Satoh [65]. It is here used to demonstrate the ability of the constitutive material models and homogenization methods, presented in Sections 1.4 to 1.6, to predict residual stress. Figure 2.7 shows a schematic illustration of two plates welded together and the three bar FE-model. The weld connecting the two plates and the heat affected zone is represented by the center bar, whereas the plates are represented by the two outer bars. To simulate the welding process and resulting residual stresses a weld-level temperature increase is prescribed to the center bar, followed by a representative cooling. The corresponding expansion and contraction of the heated bar are prevented by the outer bars, similar to how the plates prevent the heat affected zone from expanding freely.

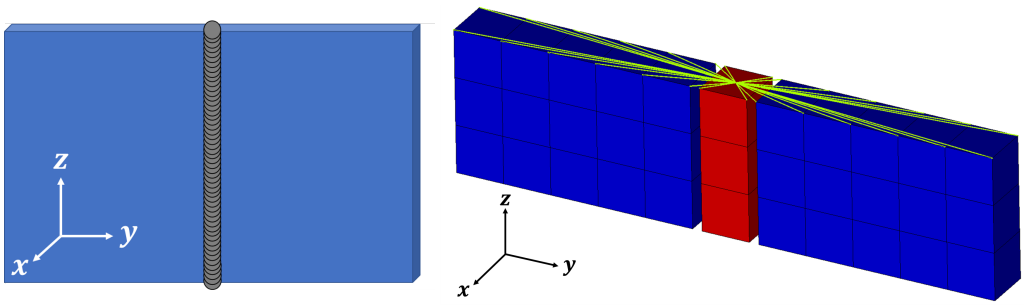


(a) (b)

Figure 2.2: *(a) Schematic illustration of two plates welded together and (b) a three bar FE model with a heated bar in red, cold bars in blue, and vertical constraint in green.*

The FE-model consists of second order 20 node brick elements. All bars are constrained vertically ($z$-direction) at the bottom end and their vertical displacements at the top end are connected via a rigid body coupling, marked by green lines in Figure 2.7b. The heated center bar is free to expand in the $x$- and $y$-direction. Based on the analytical reasoning presented by Dong [66] the size of the areas of the non-heated bars is assumed to be five times that of the heated bar. The adopted material model for the three bars is the model presented in Paper A for the pearlitic railway wheel steel ER7 (EN13262 [27]), extended with the TRIP strain model for tool steel 1.2312 (ISO4957 [67]) presented in Paper B.

The temperature load prescribed to the center bar is a smooth ramp from room

temperature to 1000°C and back to room temperature in 2 seconds. Although a cooling rate of 1000°C/s is more reminiscent of quenching than welding operations, this is used for demonstration purposes to force martensite formation. To simulate welding with a temperature load below the typical melting temperature of steel may at first glance seem odd. But it is the common practice in classical welding mechanics, cf. Lindgren [68]. At near melting temperatures the material behavior is assumed to be close to ideal-plastic, also available knowledge of mechanical behavior at these temperature levels is scarce (compared to data available at lower temperatures), whereby a simulation cut-off temperature can be motivated and generally does not impair the fidelity of the simulation outcome.

The simulation is performed using Abaqus [69] together with user subroutines developed in Papers A and B. Figure 2.3 presents the simulation results in four graphs; Starting from the bottom, the first graph presents the temperature history prescribed to the center bar. The second graph presents the time history of the material phase volume fractions, illustrating the phase transformations taking place during the rapid heating and cooling. The third graph presents the axial strain time history of the heated bar and the top graph its axial stress. The distinct kinks of the stress and strain curves are due to the limited selected temperatures used when linearly interpolating in the parameter data of the material models, see Paper A.

The results presented in the two bottom graphs of Figure 2.3 show how the prescribed temperature increase of the heated bar causes phase transformation from pearlite into austenite during heating, and from austenite into martensite during cooling. These results, combined with the restrained axial expansion generate the stress and strain results presented in the top two graphs. Evaluating the two top graphs, four stages of interest are identified; (1) heating leading up to the first phase transformation, (2) the first phase transformation, (3) the heated stage between the two phase transformations and (4) the final phase transformation and cooling.

During the first stage (1), the initial temperature increase causes the heated bar to expand, generating positive axial strain. The cool bars prevent free axial expansion of the heated bar, which thereby is subjected to compressive stress. As the temperature increases, the heated bar softens, whereby the strained cool bars start to compress the heated bar slightly. At about 0.6 seconds into the simulation, before the first phase transformation takes place, the effect of the thermal expansion again becomes dominating and the axial strain increases.

Up until the first phase transformation (2) all homogenization methods generate, as expected, identical transient stress-strain states. It is during the multi-phase stages that the effect of the different homogenization methods becomes evident. To further investigate this, stress-strain relations at 725°C for pearlite, austenite and a dual phase state with equal volume fractions of pearlite and austenite are presented in Figure 2.4.

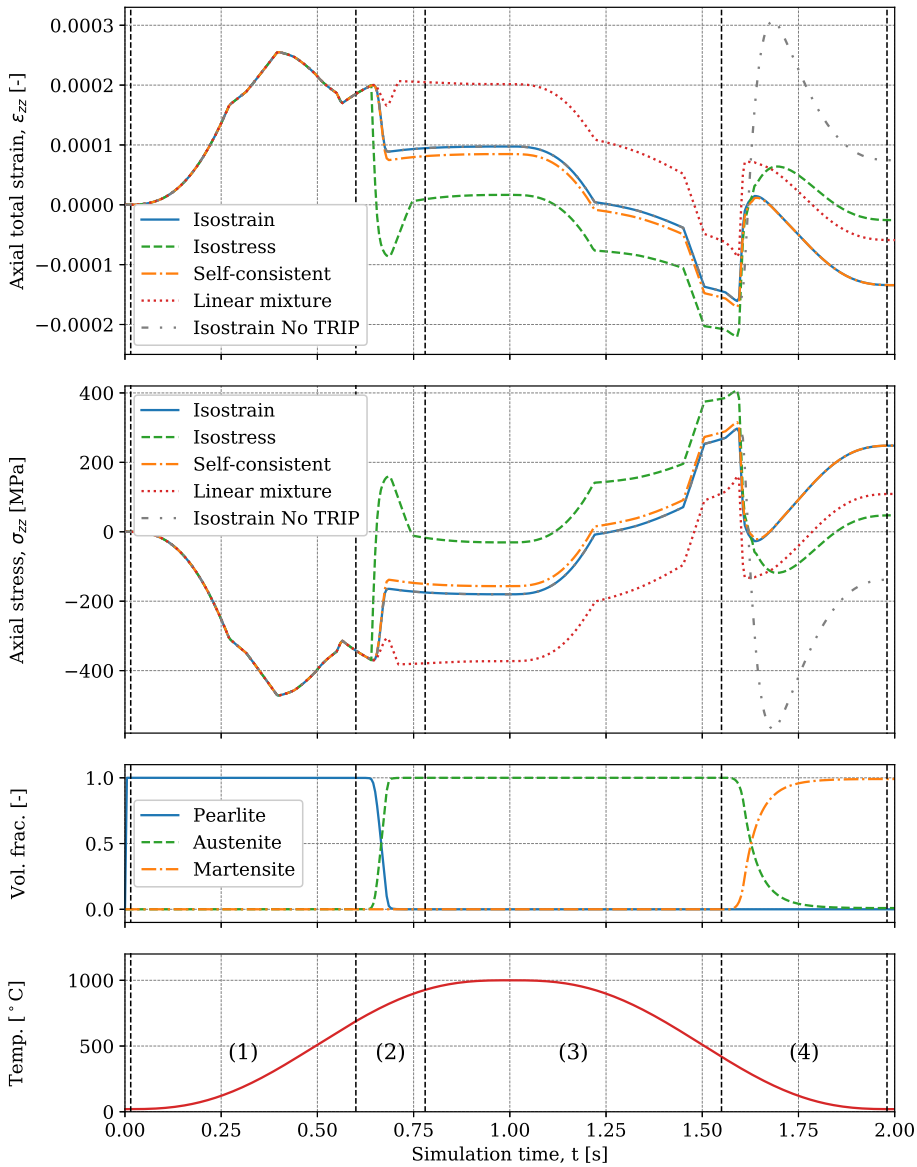


Figure 2.3: *Simulation results for heated bar. Bottom up graph description; Simulation temperature load, volume fraction, axial stress, and axial strain. Four regions are highlighted in the figure; (1) heating stage, (2) pearlite to austenite phase transformation, (3) start of cooling stage and (4) austenite to martensite phase transformation. Results are obtained from four homogenization methods, and for comparison from without the TRIP effect.*

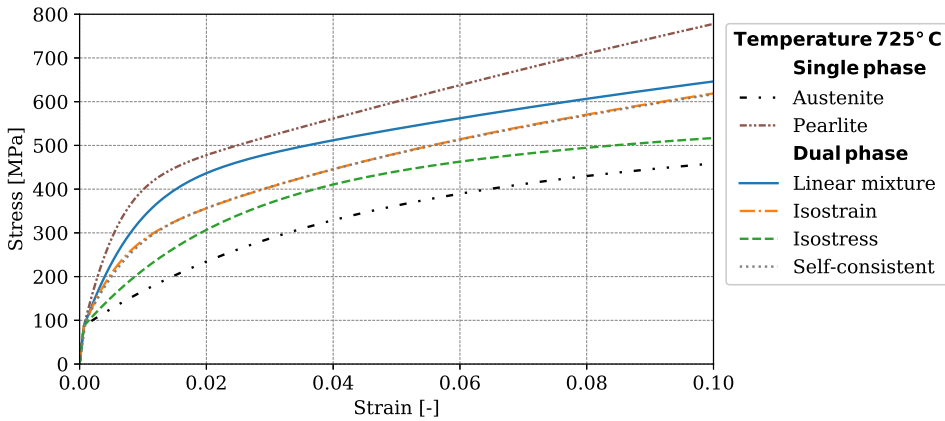


Figure 2.4: *Stress-Strain relations obtained from uniaxial load simulations at 725° C for single phase material states of austenite and pearlite and for equal composition dual phase states using different homogenization methods.*

Studying the material behavior at 725°C shows that austenite is softer than pearlite at this temperature. As the softer phase gives the larger portion of strain in the isostress homogenization method, this explains the significant change of stress and strain at stage (2) of the simulation presented in Figure 2.3. Here the isostress method generates negative strains in the system during the phase transformation. This is deemed non-physical behavior as the thermal expansion during the heating stage of the bar center should generate positive strains in the system. The isostrain and self-consistent homogenization methods generate similar results throughout the simulation, whereas the results obtained from the linear mixture rule differ. This behavior is deemed to arise due to the different yield and hardening characteristics of the linear mixture rule, see Figure 2.4. For the linear mixture rule, there is one yield surface and one hardening behavior based on the averaged material properties of the phases, whereas for the methodology of using parallel constitutive models each phase has its individual yield surface and hardening behavior.

During stage (3) of the simulation, the heated bar experiences a relatively low temperature gradient and no phase transformations take place. The stress increases as the thermal contraction in the center bar is restrained by the cool bars. The one kink at about 800°C, 1.20 seconds into the simulation is, as previously mentioned, due to scarce material data points. The negative strains seen in this stage are due to the thermal strain of austenite.

During the final stage of the simulation, stage (4) in Figure 2.3, the stress-strain state changes drastically during the martensitic phase transformation. To interpret this behavior, in terms of stress-strain relations, the material characteristics of martensite and austenite at this temperature are examined in Figure 2.5. The figure also presents homogenized characteristics of an equal composition dual phase state using the different homogenization methods.

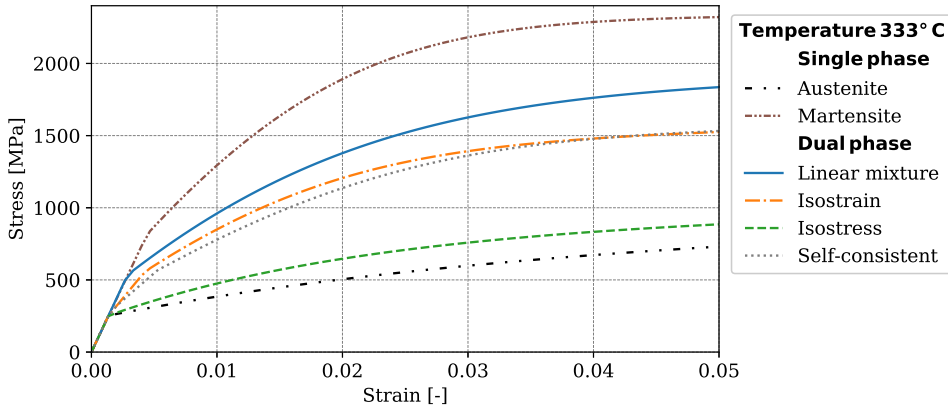


Figure 2.5: *Stress-Strain relations obtained from uniaxial load simulations at* $333^\circ C$ *for single phase material states of austenite and pearlite and for equal composition dual phase states using different homogenization methods.*

Examining the material behavior at the temperature of martensitic transformation presented in Figure 2.5 shows a substantial difference in the behavior of the two phases. With the same reasoning as discussed for the pearlite to austenite phase transformation at 725°C, this partly explains the sudden changes in the stress-strain curves at 1.6 seconds into the simulation presented in Figure 2.3. The density and thermal expansion of the two phases also play a crucial role in understanding this behavior, which is presented in further detail in the free dilatation simulations presented in Papers A and B. The TRIP strain is also a major contributor to the behavior seen during stage (4). Its impact is demonstrated in Figure 2.3 by the results obtained using the isostrain method without the TRIP strain contribution. As the deviatoric stress drives the TRIP strain evolution $\dot{\boldsymbol{\epsilon}}^{\mathrm{tp}}$, differences between the homogenization methods are magnified by the differences in their respective homogenized stress.

In summary, the three bar experiment for conceptually modeling the longitudinal residual stress in the welded plates shown in Figure 2.7a is as informative as it is simple. It is especially informative for demonstrating the impact of different homogenization methods. By the weld's idealized heating and cooling stages, the mechanisms driving the residual stress during phase transformations and restricted expansion are demonstrated. The example shows how the residual stress obtained using the four homogenization methods differs significantly, the isostrain method generates residual stress in the order of 250 MPa and the isostress method in the order of 50 MPa. In the welding mechanics literature, see e.g Masubuchi [64], the longitudinal residual stresses for this example are at the yield limit stress level. The pearlitic ER7 (EN13262 [27]) material used in this example has an initial yield limit at room temperature of 305 MPa (parameter valued adjusted to fit the cyclic material behavior), whereby the simulation models demonstrated in this example are likely to underestimate the residual stress. However, if we exclude the effects of the final phase transformation in this example, the tensile residual stress in the

heated bar will reach the yield stress level. Also, the material for the filler material may have higher yield limit, which is not accounted for in this example.

## 2.5 Moving heat source

From the three bar experiment, the next step towards a 3D welding simulation is to model the moving heat source of the wire arc welding process in the heat transfer simulation. Two common techniques found in literature are either to use prescribed nodal temperatures, see e.g. Lindgren et al. [70] and Seles et al. [71], or to use prescribed heat flux, see e.g. Deng and Murakawa [72, 73] and Taraphdar et al. [74]. Modeling of the actual arch physics is a complex research field, though it is possible, see e.g. Hu and Tsai [75], it is deemed out of scope as discussed in Section 2.2.

To simulate the heat supplied from the arc several heat distribution shapes are proposed in the literature. Common choices are the Gaussian distribution, see e.g. Eeagar and Tsai [76], a double ellipsoid distribution, see Goldak et al. [77, 78], and a conical distribution, see Spina et al. [79]. Farias et al. [80] compared the results from the three methods and found that all give valid predictions of the temperature field, with the two latter giving very similar results.

In Section 2.7, the double ellipsoid heat distribution is adopted and therefore implemented as an Abaqus [69] user subroutine with a cut-off temperature of 1000°C and a welding speed of 10 mm/s. Figure 2.6 presents a generic illustration of the heat source. As the simulation merely a first attempt at setting up a weld simulation, heat input power and the size parameters of the double ellipsoid heat distribution are adjusted such that the neighboring elements of filler elements reach the cut-off temperature.

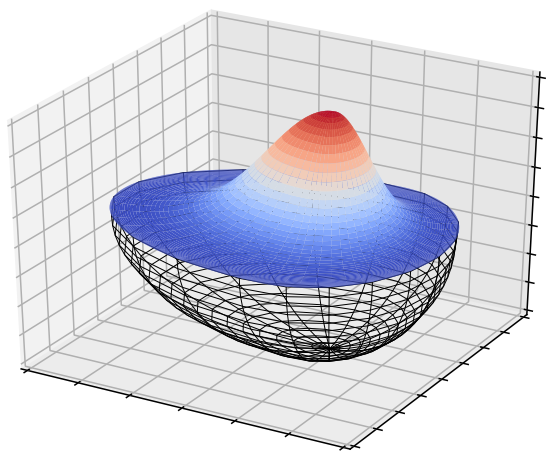

Figure 2.6: *Generic illustration of a double ellipsoid heat source. Heat affected volume illustrated by the wireframe and heat input magnitude by the colored surface.*

## 2.6 Addition of filler material in molten state

Two common approaches to addressing the continuous addition of filler material during fusion welding simulations are found in the literature, one is to use the silent (or quiet) element technique, see Lindgren et al. [70] and eg. Kollar et al. [81], the other approach is to use the element birth (or inactive) technique, see e.g. Chen et al. [82], Dong and Brust [83] or Liu et al. [84]. Studies comparing the two approaches show how both techniques generate similar temperature and stress fields for the thermal and mechanical analyses, cf. Lindgren [85].

A common approach to save computational time is to add or activate the filler elements not one by one, but lumping them into larger segments, so called macro beads, cf. Kik [86], and activating them simultaneously, see e.g. Lee et al. [55] and Lundbäck and Lindgren [87]. When simulating multi-pass welding scenarios it is also common to lump several weld passes together, see e.g. Liu et al. [88]. In the simulations in Section 2.7, the filler elements are activated individually, i.e. not using a lumped approach.

Furthermore, the quiet element approach is used in this work, where elements are activated along with the moving heat source. For the thermal simulation, quiet elements are assigned a low thermal conductivity and an initial temperature of 1000°C. When the elements are activated they are given normal thermal properties allowing them to participate in the heat transfer. The filler elements do not share nodes with the base material as these nodes are assigned room temperature initially. Therefore a contact conduction condition is introduced between the filler elements and base material elements. This is activated in the same instance as the quiet filler elements, cf. gap conductance elements used by Michaleris [89]. In this way the room temperature base material nodes are unaffected by the neighboring 1000°C quiet nodes and fictitious temperature gradients avoided.

For the mechanical simulation, the filler elements are activated as their temperatures decrease below the initial temperature of 1000°C in an attempt to mimic solidification, noting that this temperature is well below the liquidus temperature. Similar approaches are found in the literature, e.g. a study by Brust and Rybicki [90] where they used 1150°C as activation temperature. The Young's modulus of elements in the quiet state is scaled by a factor $10^{-3}$. For the filler elements to be activated in a strain free state, their reference temperature for the thermal strain, see $\boldsymbol{\epsilon}^{\text{th}}$ in Equation 1.1, is 1000°C and whatever strain that has accumulated in the quiet element is removed, similar to the proposal by Chiumenti et al. [91]. In this way spurious stresses are avoided and the contraction forces of the cooling filler material are accounted for. Using the FE mesh of the heat transfer simulation, the filler elements do not share nodes with the base material and tie contacts are used to constantly connect the surfaces. Nodal positions of the filler elements are not adjusted upon element activation, as by Lindgren and Hedblom [92] and Lundbäck and Lindgren [87]. This is reasonable if the deformations are small, which is assumed in Section 2.7.

## 2.7 Preliminary weld simulation

In this Section, FE simulations of a single weld pass in the butt welding of a plate are demonstrated. The part of the plate included in the FE-model is presented in Figure 2.7a where the two plates that are welded together are shown. The heat transfer analysis uses the pink and green parts of the FE model in Figure 2.7b, whereas the mechanical simulation uses only one of the green parts. In this way the boundary effects from the heat transfer simulation are not carried on to the mechanical simulation. Highlighted in red in Figure 2.7b is also the cross section from where results are presented. The dimensions of the heat transfer model are 170 mm x120 mm x 15 mm with the weld preparation chamfer of 10 mm depth.

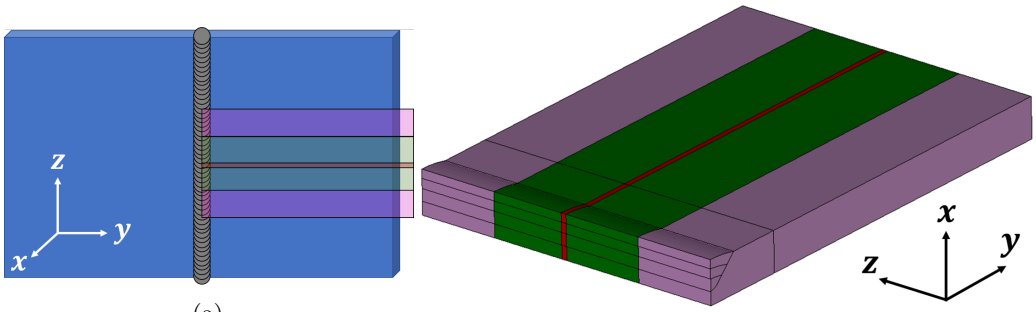


(a) (b)

Figure 2.7: *(a) Schematic illustration of two plates welded together with the symmetry FE-model highlighted (b) three pass weld FE-model, full model used in heat transfer simulation, green model used in mechanical simulation and red center-cross section used in analysis below.*

The thermo-mechanical simulations adopt the one-way coupling described in Section 1.7 and the moving heat source presented in Section 2.5. The quiet filler elements are activated with the heat source movement, see Section 2.6. Boundary conditions are surface convection with a heat transfer coefficient of 25 W/m$^2$K and surface radiation with an emissivity coefficient of 0.2, on both the top and bottom of the plate. Initial temperature and surrounding room temperature are set to 25°C. The FE model has been prepared for three passes of butt welding, but results will only be presented for a single pass.

In the mechanical simulation, symmetry boundary conditions are applied for the $x-z$ plane through the center of the plate and weld, as well as for the $x-y$ planes at the transverse plate edges. The coordinate system is presented in Figure 2.7b. The plate edge opposite to the weld is unconstrained and rigid body motion in the $x$-direction is prevented. The material used is the same as in the three-bar example. Note then, that the weld filler material and the plate are assumed to have the same material properties. The simulation is run in Abaqus [69] together with the user subroutines described above and it accounts for geometric nonlinearity.

Figure 2.8 presents the temperature field that is mapped onto the mechanical simulation. Quiet elements not yet activated are hidden, demonstrating how filler material elements are activated when the temperature drops below 1000°C in the mechanical simulation. The rather steep temperature gradients seen in the model could indicate a need for refining the FE mesh, see Figure 2.9.

The phase transformations following the first weld pass are shown in Figure 2.9, where the martensite volume fraction is presented for the center cross-section highlighted in red in Figure 2.7. A martensite volume fraction of zero represents pearlite. The figure also presents the data point, P1, from where the stress-history will be presented. The model predicts significant martensite formation in the weld material and in the heat affected zone. The somewhat irregular shape of the transition between martensite to pearlite, again, indicates the need for mesh refinement.

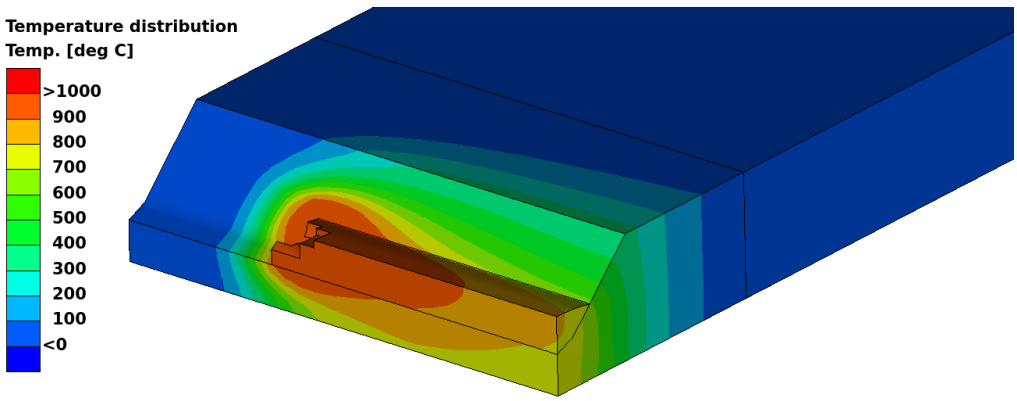


Figure 2.8: *Heat transfer simulation results, temperature distribution with the silent elements hidden.*

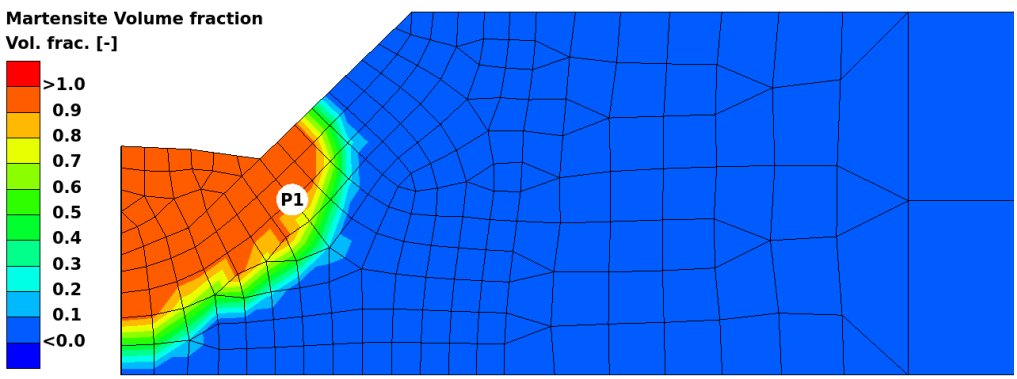


Figure 2.9: *Residual volume fraction martensite, FE-mesh and data point P1 used for stress history results*

The longitudinal residual stress along a path in the transverse ($y$)-direction at the center of the plate thickness is presented in Figure 2.10. To evaluate the cause and correlation between the different features of the material model and the obtained results, residual stresses from four simulations; (1) a simulation with all features presented in Sections 1.4 to 1.6 included in the model and using the linear mixture rule homogenization method, (2) a simulation without the TRIP strain $\boldsymbol{\epsilon}^{\text{tp}}$ implemented in the model, (3) a simulation including all features where the plate is heated to 500°C during the welding procedure, and (4) a simulation without any phase transformation kinetics included, i.e. simply heating and cooling of pearlite. A limitation in the simulations is that only the material model with the linear mixture rule has been used so far.

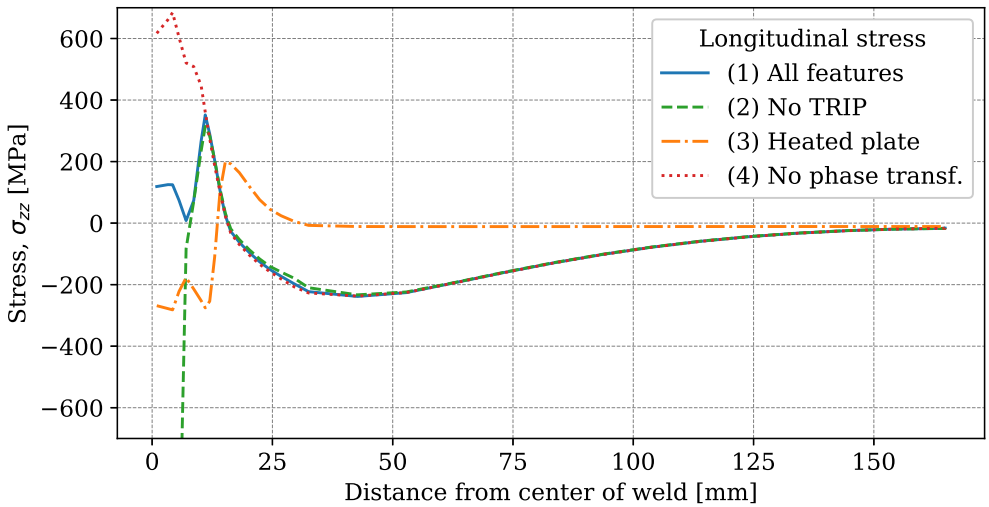


Figure 2.10: *Transverse variation of the residual longitudinal stress at the center of the plate, measured from the weld towards the free end of the plate.*

By evaluating the overall trends of the results presented in Figure 2.10 it can be concluded that the far-field material is unaffected by the welding as the stresses are negligible for all simulations. Furthermore, for simulation (1) and (4) the material in the heat affected zone, i.e. the martensitic region shown in Figure 2.9, experiences tensile stresses and the neighboring region experiences compressive stresses. By comparing the results from (4) with the other simulations it can be observed that by accounting for phase transformations, the longitudinal stress is decreased due to the related volume change. As the martensitic transformation takes place in a state of tensile stresses, the TRIP strain $\boldsymbol{\epsilon}^{\text{tp}}$ becomes positive, thus generating positive stresses changes during the phase transformation, as seen in both Figures 2.3 and 2.10. For the heated plate simulation, the transformation induced strains cause compressive residual stresses in the weld a small effect in the surrounding material.

Figure 2.11 presents three graphs, the top graph the history of longitudinal stress for during the four simulations measured in point P1 in Figure 2.3. The two bottom

graphs presents the phase fraction evolutions and temperature for the non-heated plate simulations. These graphs show how the intense heating and rapid cooling causes austenitization and martensite formation. The top graph complements the reasoning regarding the results presented in Figure 2.10 by demonstrating the role of the different features in the model during phase transformations, i.e. the residual longitudinal stress level will vary considerably depending on the material model used. Note that for the heated plate simulation, the heated austenite does not transform into martensite, but back into pearlite.

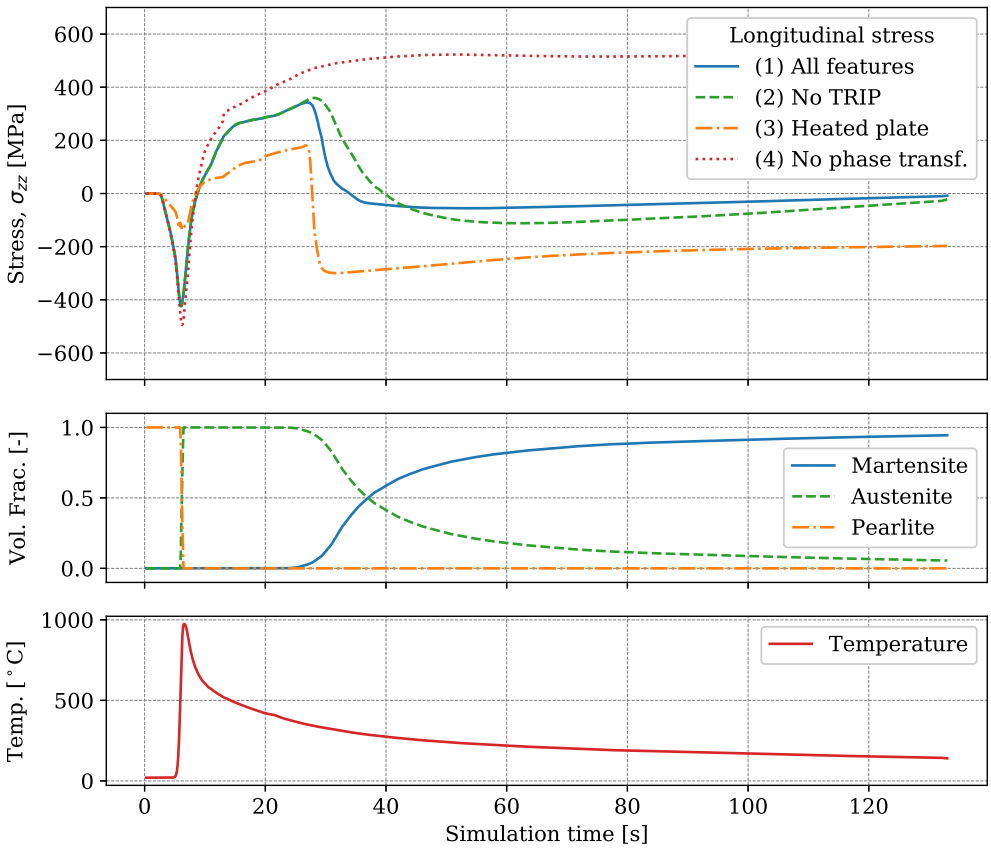


Figure 2.11: *History data measured in point P1 in Figure 2.9 Top graph: Longitudinal stress, middle graph: phase fractions and bottom graph: temperature*

# 3 Conclusions and outlook

## 3.1 Conclusions

Homogenization based macroscopic material models incorporating cyclic plasticity and phase transformations were developed for thermo-mechanically loaded pearlitic steels. For heating events, the phase transformations that have been accounted for are austenitization and tempering of martensite, and for cooling events transformation from austenite into pearlite, bainite or martensite. Cyclic plasticity was incorporated in the model by using a Chaboche plasticity model with a von Mises yield function, non-linear isotropic and kinematic hardening.

The models have been applied to railway related heating events in both Papers A and B. Paper A presents an FE simulation of a double wheel flat loading on the tread of a railway wheel. By simulating the repeated heating it is demonstrated how small regions of primary and secondary martensite are formed and how some regions becomes tempered when peak temperatures are lower. The following mechanical analysis shows that compressive residual stresses are obtained in the primary martensitic layer due to its volume expansion and that tensile residual stresses are obtained in the tempered martensite layer. High contact loads are imposed onto the wheel tread to study how the residual stresses from the thermal loads are affected by over-rollings. The simulation shows how the maximum principal stress close to the surface tends to decrease. Whereas the stresses in the tempered martensite layer stabilize at very high levels. The tempered martensite is still rather brittle and therefore susceptible to crack initiation during the high stress levels indicated by the simulation results. This has also been experimentally observed in micrographs of a double wheel flat by Ahlström and Karlsson [45] where micro-cracks were identified.

By extending the plasticity model to also account for the effect of transformation induced plasticity, more accurate predictions of residual stresses are obtained, as is demonstrated in Paper B. This work also evaluates the influence of the choice of homogenization method. Moreover, the four homogenization methods studied show different behavior during the multi-phase stages in the simulated laser heated rail surface experiment, which in turn generates different residual stress states. There is also a significant difference between the methods in terms of numerical stability and computational cost. All things considered, the self-consistent method shows the most promising performance as it is numerically stable and is relatively computationally efficient, but mainly since it generates results that are slightly more similar to experimental measurements available so far.

As a step towards FE simulations of repair welding of rails, butt welding of two plates has been simulated. Implemented as Abaqus user subroutines, the butt welding simulation includes a moving heat source in the shape of a double ellipsoid and continuous addition of filler material using the quiet element approach. The material model with phase transformations and plasticity developed in Papers A and B has been used for the filler material and plates. The simulations show how the model is able to reproduce the general residual stress behavior found in the literature, i.e. tensile residual stresses in the heat affected zone and compressive stresses neighboring regions. These are promising

results that can be used as a base for future work regarding simulations of repair welding.

## 3.2 Outlook

In the work presented in Papers A and B, and in this Extended Summary of the thesis, there are some questions left unanswered, there are several aspects that are simplified in the modeling and the weld simulation is still in its very beginning. However, the simulation methodologies of using homogenization techniques and individual constitutive models for the phases have proven to be quite versatile, whereby the framework opens the door for future extensions and additions of modeling features. Examples of such features and aspects that might need to be accounted for in future studies include are:

- The influence of the choice of homogenization method in welding simulations should be studied.
- The interaction between a recently nucleated phase and its parent phase in terms of plasticity and hardening inheritance should be investigated.
- Due to the cyclic thermal effects of multi-pass repair welding thermal recovery effects, i.e. annealing could be necessary to incorporate in the material model.
- The heat transfer simulation should be extended to account for latent heat during phase transformations. It is shown by Ahlström and Karlsson [13] that the influence of latent heat is considerable when the cooling rate is relatively slow, whereby this might be relevant in the welding simulations.
- Simulations need to be calibrated to experimental results to ensure that the results are reliable. This is especially true for welding as the predictive nature of welding simulations is limited without precise tuning of the heat input.
- Results from welding simulations using the presented material models and methodologies should be compared with results obtained from commercial welding simulating software.

# References


[1] J.-P. Rodrigue, C. Comtois, and B. Slack. *The geography of transport systems*. Vol. Fourth edition. Routledge, 2016.

[2] C. Doll, C. Brauer, J. Köhler, and P. Scholten. *Methodology for GHG Efficiency of Transport Modes*. Karlsruhe, Germany: Fraunhofer-Institute for Systems and Innovation Research ISI, 2020.

[3] *White paper: Roadmap to a Single European Transport Area – Towards a competitive and resource efficient transport system*. Brussels: European Commision (EC), 2011.

[4] *Commission Communication: A Roadmap for moving to a competitive low carbon economy in 2050*. Brussels: European Commision (EC), 2011.

[5] *Track Maintenance & Renewal*. EIM-EFRTC-CER Working Group, 2012.
[6] T. Lidén and M. Joborn. Dimensioning windows for railway infrastructure maintenance: Cost efficiency versus traffic impact. *Journal of Rail Transport Planning Management* 6.1 (2016), 32–47.
[7] S. Kallander. Trafikverket, Personal Communication, Apr. 27, 2021.
[8] C. Jessop, J. Ahlström, C. Persson, and Y. Zhang. Damage evolution around white etching layer during uniaxial loading. *Fatigue & Fracture of Engineering Materials & Structures* 43.1 (2020), 201–208.
[9] S. Niederhauser, B. Karlsson, and P. Sotkovszki. Microstructural development in the heat-affected zone of a laser-cladded steel. *Zeitschrift fuer Metallkunde* 96 (4 2005).
[10] J. Ahlström and B. Karlsson. Analytical 1D model for analysis of the thermally affected zone formed during railway wheel skid. *Wear* 232.1 (1999), 15–24.
[11] A. Esmaeili, M. S. Walia, K. Handa, K. Ikeuchi, M. Ekh, T. Vernersson, and J. Ahlström. A methodology to predict thermomechanical cracking of railway wheel treads: From experiments to numerical predictions. *International Journal of Fatigue* 105.Supplement C (2017), 71–85.
[12] J. Jergéus. Martensite formation and residual stresses around railway wheel flats. *Proceedings of the Institution of Mechanical Engineers, Part C: Journal of Mechanical Engineering Science* 212.1 (1998), 69–79.
[13] J. Ahlström and B. Karlsson. Modelling of heat conduction and phase transformations during sliding of railway wheels. *Wear* 253.1 (2002), 291–300.
[14] H. Bhadeshia and R. Honeycombe. *Steels: Microstructure and Properties*. Butterworth-Heinemann, 2017.
[15] E. Pereloma and D. Edmonds. *Phase Transformations in Steels. Volume 1: Fundamentals and Diffusion-Controlled Transformations*. Cambridge: Woodhead Publishing Limited, 2012.
[16] E. Pereloma and D. Edmonds. *Phase Transformations in Steels. Volume 2: Diffusionless transformations, high strength steels, modelling and advanced analytical techniques*. Cambridge: Woodhead Publishing Limited, 2012.
[17] D. Raabe. *Computational Materials Science - The Simulation of Materials, Microstructures and Properties*. Wiley-VCH Verlag, 1998.
[18] J. Lin, D. Balint, and M. Pietrzyk. *Microstructure Evolution in Metal Forming Processes*. Woodhead Publishing, 2012, pp. 1–394.
[19] J. F. Archard, R. A. Rowntree, and K. L. Johnson. Metallurgical phase transformations in the rubbing of steels. *Proceedings of the Royal Society of London. A. Mathematical and Physical Sciences* 418.1855 (1988), 405–424.
[20] S. Denis, D. Farias, and A. Simon. Mathematical Model Coupling Phase Transformations and Temperature Evolutions in Steels. *ISIJ International* 32.3 (1992), 316–325.
[21] F. M. B. Fernandes, S. Denis, and A. Simon. Mathematical model coupling phase transformation and temperature evolution during quenching of steels. *Materials Science and Technology* 1.10 (1985), 838–844.
[22] E. Scheil. Anlaufzeit der austenitumwandlung. *Archiv für das Eisenhüttenwesen* 8.12 (1935), 565–567.

[23] C. Verdi and A. Visintin. A mathematical model of the austenite-pearlite transformation in plain carbon steel based on the Scheil's additivity rule. *Acta Metallurgica* 35.11 (1987), 2711–2717.

[24] D. Koistinen and R. Marburger. A general equation prescribing the extent of the austenite-martensite transformation in pure iron-carbon alloys and plain carbon steels. *Acta Metallurgica* 7.1 (1959), 59–60.

[25] K. Cvetkovski, J. Ahlström, and B. Karlsson. Influence of short heat pulses on properties of martensite in medium carbon steels. *Materials Science and Engineering: A* 561 (2013), 321–328.

[26] J. Chaboche. Constitutive equations for cyclic plasticity and cyclic viscoplasticity. *International Journal of Plasticity* 5.3 (1989), 247–302.

[27] Railway applications - Wheelsets and bogies - Wheels - Product requirement. EN 13262:2004+A1. Brussels: European Committee for Standardization (CEN), 2004.

[28] R. Mahnken, A. Schneidt, and T. Antretter. Macro modelling and homogenization for transformation induced plasticity of a low-alloy steel. *International Journal of Plasticity* 25.2 (2009), 183–204.

[29] C. O. Frederick and P. J. Armstrong. A mathematical representation of the multiaxial Bauschinger effect. *Materials at High Temperatures* 21.1 (2014), 1–26.

[30] D. Nikas, J. Ahlström, and A. Malakizadi. Mechanical properties and fatigue behaviour of railway wheel steels as influenced by mechanical and thermal loadings. *Wear* 366-367.Supplement C (2016), 407–415.

[31] Sente-Software. *JMatPro 6.0, 2018*. Version 6.0. May 25, 2018.

[32] C. Şimşir and C. H. Gür. A FEM based framework for simulation of thermal treatments: Application to steel quenching. *Computational Materials Science* 44.2 (2008), 588–600.

[33] S. Denis, S. Sjöstrom, and A. Simon. Coupled Temperature, Stress, Phase Transformation Calculation Model Numerical Illustration of the Internal Stresses Evolution during Cooling of a Eutectoid Carbon Steel Cylinder. *Metallurgical Transactions A* 18.July (1987), 1203–1212.

[34] F. Fischer, G. Reisner, E. Werner, K. Tanaka, G. Cailletaud, and T. Antretter. A new view on transformation induced plasticity (TRIP). *International Journal of Plasticity* 16.7 (2000), 723–748.

[35] R. G. Stringfellow, D. M. Parks, and G. B. Olson. A constitutive model for transformation plasticity accompanying strain-induced martensitic transformations in metastable austenitic steels. *Acta Metallurgica Et Materialia* 40.7 (1992), 1703–1716.

[36] O. Bouaziz and P. Buessler. Iso-work increment assumption for heterogeneous material behavior modelling. *Advanced Engineering Materials* 6.1-2 (2004), 79–83.

[37] J. D. Eshelby. The determination of the elastic field of an ellipsoidal inclusion, and related problems. *Proceedings of the royal society of London. Series A. Mathematical and physical sciences* 241.1226 (1957), 376–396.

[38] J. Hutchinson. Elastic-plastic behaviour of polycrystalline metals and composites. *Proceedings of the Royal Society A: Mathematical, Physical and Engineering Sciences* 319 (1970), 247–272.

[39] R. A. Lebensohn, P. A. Turner, J. W. Signorelli, and G. R. Canova. Calculation of intergranular stresses based on a large-strain viscoplastic self-consistent polycrystal

model. *Modelling and Simulation in Materials Science and Engineering* 6.April 1998 (1998), 447–465.

[40] M. Coret and A. Combescure. A mesomodel for the numerical simulation of the multiphasic behavior of materials under anisothermal loading (application to two low-carbon steels). *International Journal of Mechanical Sciences* 44.9 (2002), 1947–1963.

[41] L. Börjesson and L.-E. Lindgren. Simulation of multipass welding with simultaneous computation of material properties. *Journal of Engineering Materials and Technology, Transactions of the ASME* 123.1 (2001), 106–111.

[42] L.-E. Lindgren. "Modelling for residual stresses and deformations due to welding : "knowing what isn't necessary to know"." *Mathematical Modelling of Weld Phenomena 6 :* Maney Publishing (for The Institute of Materials, Minerals and Mining), 2002, pp. 491–518.

[43] P. Dong. Residual stresses and distortions in welded structures: a perspective for engineering applications. *Science and Technology of Welding and Joining* 10.4 (2005), 389–398.

[44] S. Edalatpour, A. Saboonchi, and S. Hassanpour. Effect of phase transformation latent heat on prediction accuracy of strip laminar cooling. *Journal of Materials Processing Technology* 211.11 (2011), 1776–1782.

[45] J. Ahlström and B. Karlsson. Microstructural evaluation and interpretation of the mechanically and thermally affected zone under railway wheel flats. *Wear* 232.1 (1999), 1–14.

[46] C. Jessop. "Damage and defects in railway materials. Influence of mechanical and thermal damage on crack initiation and propagation". PhD thesis. Chalmers University of Technology, 2019.

[47] R. R. Porcaro, G. L. Faria, L. B. Godefroid, G. R. Apolonio, L. C. Cândido, and E. S. Pinto. Microstructure and mechanical properties of a flash butt welded pearlitic rail. *Journal of Materials Processing Technology* 270 (2019), 20–27.

[48] A. Skyttebol and B. L. Josefson. "Numerical simulation of flash butt welding of railway rails". *Mathematical modelling of weld phenomena 7*. Ed. by H. Cerjak, H. K. D. H. Bhadeshia, and E. Kozeschnik. Graz, Austria: Verlag der Technischen Universität Graz, 2005, pp. 943–964.

[49] D. Tawfik, P. J. Mutton, O. Kirstein, and W. K. Chiu. A comparative study between FEA, trepanning and neutron strain diffraction on residual stresses in flash-butt welded rails. *Journal of Neutron Research* 15.3-4 (2007), 199–205.

[50] B. L. Josefson, R. Bisschop, M. Messaadi, and J. Hantusch. Residual stresses in thermite welded rails: significance of additional forging. *Welding in the World* 64.7 (2020), 1195–1212.

[51] I. Salehi, A. Kapoor, and P. Mutton. Multi-axial fatigue analysis of aluminothermic rail welds under high axle load conditions. *International Journal of Fatigue* 33.9 (2011), 1324–1336.

[52] A. Skyttebol, B. Josefson, and J. Ringsberg. Fatigue crack growth in a welded rail under the influence of residual stresses. *Engineering Fracture Mechanics* 72.2 (2005). Fracture Mechanics in Railway Applications, 271–285.

[53] B. L. Josefson. “Welding of rails and effects of crack initiation and propagation”. *Encyclopedia of Thermal Stresses*. Ed. by R. B. Hetnarski. Rochester, USA: Springer, Dordrecht, 2014, pp. 6589–6594.

[54] E. Kabo, A. Ekberg, and M. Maglio. Rolling contact fatigue assessment of repair rail welds. *Wear* 436-437 (2019), 203030.

[55] S.-H. Lee, S. H. Kim, Y.-S. Chang, and H. K. Jun. Fatigue life assessment of railway rail subjected to welding residual and contact stresses. *Journal of Mechanical Science and Technology* 28.11 (2014), 4483–4491.

[56] K. Runesson, A. Skyttebol, and L.-E. Lindgren. “3.05 - Nonlinear Finite Element Analysis and Applications to Welded Structures”. *Comprehensive Structural Integrity*. Ed. by I. Milne, R. Ritchie, and B. Karihaloo. Oxford: Pergamon, 2003, pp. 255–320.

[57] L.-E. Lindgren. *Computational welding mechanics*. Woodhead Publishin Limitedg, 2007.

[58] J. A. Goldak and M. Akhlaghi. *Computational welding mechanics*. Springer Science & Business Media, 2005.

[59] C. L. Magee. “Transformation kinetics, microplasticity and aging of martensite in Fe-31Ni”. PhD thesis. Carnegie Institute of Technology, Pittsburgh, Pa, 1966.

[60] A. Oddy, J. McDill, and L. Karlsson. Microstructural predictions including arbitrary thermal histories, reaustenization and carbon segregation effects. *Canadian Metallurgical Quarterly* 35.3 (1996), 275–283.

[61] M. Wolff, M. Böhm, and B. Suhr. Comparison of different approaches to transformation-induced plasticity in steel. *Materialwissenschaft und Werkstofftechnik: Entwicklung, Fertigung, Prüfung, Eigenschaften und Anwendungen technischer Werkstoffe* 40.5-6 (2009), 454–459.

[62] F. D. Fischer, Q.-P. Sun, and K. Tanaka. Transformation-Induced Plasticity (TRIP). *Applied Mechanics Reviews* 49.6 (June 1996), 317–364.

[63] A. S. Oddy, J. A. Goldak, and J. M. McDill. Transformation plasticity and residual stresses in single-pass repair welds. *Journal of Pressure Vessel Technology, Transactions of the ASME* 114.1 (1992), 33–38.

[64] K. Masubuchi. *Analysis of welded structures: residual stresses, distortion, and their consequences*. Vol. First edition. Elmsford (New York): Pergamon Press Inc., 1980.

[65] K. Satoh. Transient thermal stresses of weld heat-affected zone by both-ends-fixed bar analogy. *Transactions of the Japan Welding Society* 3.1 (1972), 125–134.

[66] P. Dong. On repair weld residual stresses and significance to structural integrity. *Welding in the World* 62.2 (2018), 351–362.

[67] International standard ISO 4957:2018(E) - Tool Steels. Geneva,Switzerland: (the International Organization for Standardization (ISO), 2018.

[68] L.-E. Lindgren. Finite element modeling and simulation of welding Part 2: Improved material modeling. *Journal of Thermal Stresses* 24 (2001), 195–231.

[69] *Abaqus Analysis User’s Manual*. 2018th ed. Providence, Rhode Island USA: Dassault Systèmes Simulia Corp, 2018.

[70] L.-E. Lindgren, H. Runnemalm, and M. O. Näsström. Simulation of multipass welding of a thick plate. *International Journal for Numerical Methods in Engineering* 44.9 (1999), 1301–1316.

[71] K. Seleš, M. Perić, and Z. Tonković. Numerical simulation of a welding process using a prescribed temperature approach. *Journal of Constructional Steel Research* 145 (2018), 49–57.

[72] D. Deng and H. Murakawa. Numerical simulation of temperature field and residual stress in multi-pass welds in stainless steel pipe and comparison with experimental measurements. *Computational Materials Science* 37.3 (2006), 269–277.

[73] D. Deng and H. Murakawa. Finite element analysis of temperature field, microstructure and residual stress in multi-pass butt-welded 2.25Cr–1Mo steel pipes. *Computational Materials Science* 43.4 (2008), 681–695.

[74] P. K. Taraphdar, R. Kumar, C. Pandey, and M. M. Mahapatra. Significance of Finite Element Models and Solid-State Phase Transformation on the Evaluation of Weld Induced Residual Stresses. *Metals and Materials International* 27.9 (2021), 3478–3492.

[75] J. Hu and H. Tsai. Heat and mass transfer in gas metal arc welding. Part I: The arc. *International Journal of Heat and Mass Transfer* 50.5 (2007), 833–846.

[76] T. Eagar and N. Tsai. Temperature fields produced by traveling distributed heat sources. *Welding journal* 62.12 (1983), 346–355.

[77] J. Goldak, A. Chakravarti, and M. Bibby. A New Finite Element Model for Welding Heat Sources. *Metallurgical Transactions B* 15.June (1984), 299–305.

[78] J. Goldak, M. Bibby, J. Moore, R. House, and B. Patel. Computer modeling of heat flow in welds. *Metallurgical transactions B* 17.3 (1986), 587–600.

[79] R. Spina, L. Tricarico, G. Basile, and T. Sibillano. Thermo-mechanical modeling of laser welding of AA5083 sheets. *Journal of Materials Processing Technology* 191.1 (2007). Advances in Materials and Processing Technologies, July 30th - August 3rd 2006, Las Vegas, Nevada, 215–219.

[80] R. Farias, P. Teixeira, and L. Vilarinho. An efficient computational approach for heat source optimization in numerical simulations of arc welding processes. *Journal of Constructional Steel Research* 176 (2021), 106382.

[81] D. Kollár, B. Kövesdi, L. G. Vigh, and S. Horváth. Weld process model for simulating metal active gas welding. *International Journal of Advanced Manufacturing Technology* 102.5-8 (2019), 2063–2083.

[82] B.-Q. Chen, M. Hashemzadeh, and C. Guedes Soares. Numerical and experimental studies on temperature and distortion patterns in butt-welded plates. *International Journal of Advanced Manufacturing Technology* 72.5-8 (2014), 1121–1131.

[83] P. Dong and F. W. Brust. Welding Residual Stresses and Effects on Fracture in Pressure Vessel and Piping Components: A Millennium Review and Beyond. *Journal of Pressure Vessel Technology* 122.3 (2000), 329–338.

[84] C. Liu, J. Zhang, and C. Xue. Numerical investigation on residual stress distribution and evolution during multipass narrow gap welding of thick-walled stainless steel pipes. *Fusion Engineering and Design* 86.4 (2011), 288–295.

[85] L.-E. Lindgren. Finite element modeling and simulation of welding part 1: Increased complexity. *Journal of Thermal Stresses* 24.2 (2001), 141–192.

[86] T. Kik. Computational Techniques in Numerical Simulations of Arc and Laser Welding Processes. *Materials* 13.3 (2020).

[87] A. Lundbäck and L.-E. Lindgren. Modelling of metal deposition. *Finite Elements in Analysis and Design* 47.10 (2011), 1169–1177.

[88] C. Liu, Y. Luo, M. Yang, and Q. Fu. Three-dimensional finite element simulation of welding residual stress in RPV with two J-groove welds. English. *Welding in the World* 61.1 (Oct. 2017), 151–160.

[89] P. Michaleris. Residual stress distributions for multi-pass welds in pressure vessel and piping components. *ASME-PUBLICATIONS-PVP* 327 (1996), 17–28.

[90] F. W. Brust and E. F. Rybicki. A Computational Model of Backlay Welding for Controlling Residual Stresses in Welded Pipes. *Journal of Pressure Vessel Technology* 103.3 (Aug. 1981), 226–232.

[91] M. Chiumenti, M. Cervera, A. Salmi, C. Agelet de Saracibar, N. Dialami, and K. Matsui. Finite element modeling of multi-pass welding and shaped metal deposition processes. *Computer Methods in Applied Mechanics and Engineering* 199.37 (2010), 2343–2359.

[92] L.-E. Lindgren and E. Hedblom. Modelling of addition of filler material in large deformation analysis of multipass welding. *Communications in Numerical Methods in Engineering* 17.9 (2001), 647–657.

# Part II
# Appended Papers A-B

# Paper A

**Modelling of cyclic plasticity and phase transformations during repeated localheating events in rail and wheel steels**

# Paper B

**Homogenization based macroscopic model of phase transformations and cyclic plasticity in pearlitic steel**